Article

Immunity

Lysosomal endonuclease RNase T2 and PLD exonucleases cooperatively generate RNA ligands for TLR7 activation

Graphical abstract

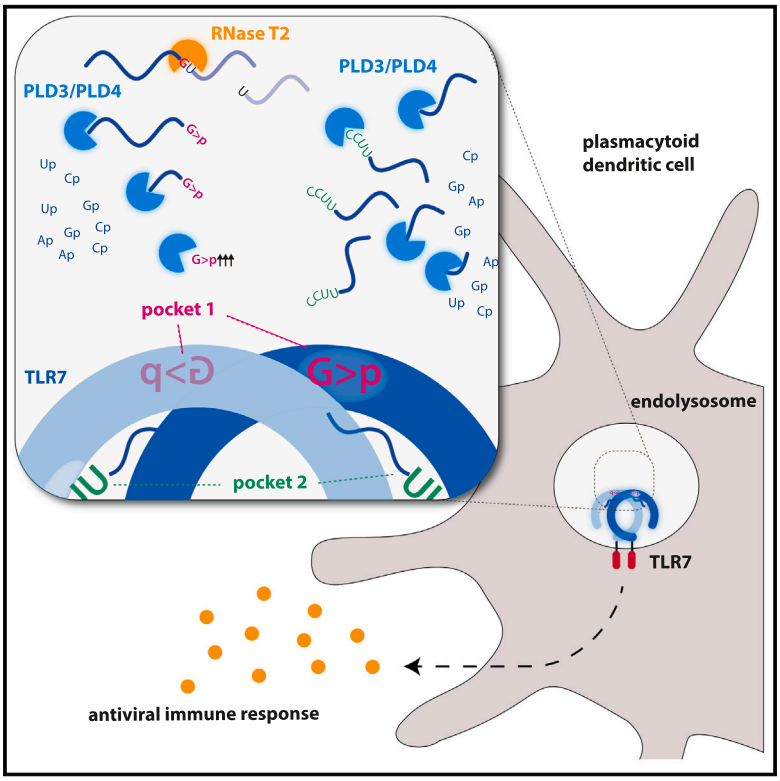

Highlights

- RNase T2 and PLD exonucleases process RNA upstream of TLR7
- PLD exonucleases release terminal 2′,3′-cyclic GMPs to engage TLR7 pocket 1
- PLD enzymes are also critical to generate RNA fragments for TLR7 pocket 2
- PLDs dimer formation is needed for RNA substrate processing

Authors

Marleen Bérouti, Katja Lammens, Matthias Heiss, ..., Thomas Carell, Karl-Peter Hopfner, Veit Hornung

Correspondence

hornung@genzentrum.lmu.de

In brief

TLR7 is critical for recognizing RNA virus infection and initiating antiviral responses. Bérouti et al. demonstrate how RNase T2 and PLD exonucleases generate RNA fragments for TLR7 activation, thus providing insights into immune recognition of exogenous RNAs, with potential therapeutic implications.

Bérouti et al., 2024, Immunity *57*, 1482–1496
July 9, 2024
https://doi.org/10.1016/j.immuni.2024.04.010

CellPress

CellPress
OPEN ACCESS

Immunity

Article

Lysosomal endonuclease RNase T2 and PLD exonucleases cooperatively generate RNA ligands for TLR7 activation

Marleen Bérouti,[1] Katja Lammens,[1] Matthias Heiss,[2] Larissa Hansbauer,[1] Stefan Bauernfried,[1] Jan Stöckl,[1] Francesca Pinci,[1] Ignazio Piseddu,[1,3] Wilhelm Greulich,[1] Meiyue Wang,[1] Christophe Jung,[1] Thomas Fröhlich,[1] Thomas Carell,[2] Karl-Peter Hopfner,[1] and Veit Hornung[1,4,*]

[1]Gene Center and Department of Biochemistry, Ludwig-Maximilians-Universität, Munich, Germany
[2]Department of Chemistry, Ludwig-Maximilians-Universität, Munich, Germany
[3]Department of Medicine II, University Hospital Munich, Munich, Germany
[4]Lead contact
*Correspondence: hornung@genzentrum.lmu.de
https://doi.org/10.1016/j.immuni.2024.04.010

SUMMARY

Toll-like receptor 7 (TLR7) is essential for recognition of RNA viruses and initiation of antiviral immunity. TLR7 contains two ligand-binding pockets that recognize different RNA degradation products: pocket 1 recognizes guanosine, while pocket 2 coordinates pyrimidine-rich RNA fragments. We found that the endonuclease RNase T2, along with 5′ exonucleases PLD3 and PLD4, collaboratively generate the ligands for TLR7. Specifically, RNase T2 generated guanosine 2′,3′-cyclic monophosphate-terminated RNA fragments. PLD exonuclease activity further released the terminal 2′,3′-cyclic guanosine monophosphate (2',3'-cGMP) to engage pocket 1 and was also needed to generate RNA fragments for pocket 2. Loss-of-function studies in cell lines and primary cells confirmed the critical requirement for PLD activity. Biochemical and structural studies showed that PLD enzymes form homodimers with two ligand-binding sites important for activity. Previously identified disease-associated PLD mutants failed to form stable dimers. Together, our data provide a mechanistic basis for the detection of RNA fragments by TLR7.

INTRODUCTION

Toll-like receptor 7 (TLR7) is a key sentinel of the innate immune system that plays a critical role in detecting non-self RNA,[1,2] primarily from viral sources.[3,4] At the same time, TLR7 can also be erroneously activated by endogenous RNA, which has been implicated in the pathogenesis of several autoimmune diseases.[5] Indeed, TLR7 activation must be tightly balanced, and much progress has been made in understanding the regulation of TLR7 responses at the level of the receptor and also its subcellular compartment, which plays an important role in regulating its activity.[6,7] However, the exact process by which RNA is made "visible" to TLR7 remains unclear. TLR7 is highly expressed in plasmacytoid dendritic cells (pDCs), positioning these cells as central players in RNA-mediated immune surveillance and response.[8] TLR7 and its homolog TLR8 are positioned as homodimers in the endolysosomal compartment according to a rotational symmetry axis, while their leucine-rich repeat (LRR) ligand-binding domains face the lumen. Structural studies have identified two distinct bindings pockets that engage with distinct types of RNA molecules. TLR7 binds to guanosine with its first binding pocket, whereas the second binding pocket engages with pyrimidine-rich oligoribonucleotides (ORNs) that preferably contain two consecutive uridine nucleotides.[9,10] TLR8, on the other hand, binds to uridine with the first binding pocket, yet detects purine-terminated ORN fragments with the second binding pocket.[11] The engagement of the second binding pocket allosterically increases the affinity of the first binding pocket toward its ligand. The first binding pocket lies within the dimerization interface of these TLRs, and agonistic ligands within this pocket bridge the two TLR molecules. In the case of TLR7, this event results in the stable dimerization of this receptor and thereby results in the formation of a signaling-competent state. Interestingly, biochemical studies have shown that guanosine 2′,3′-cyclic monophosphate (2',3'-cGMP) is a high-affinity ligand for the first pocket of TLR7,[10] suggesting that it may be an endogenous agonist for TLR7.

We and others have found that the endolysosomal nuclease RNase T2 is indispensable for TLR8 activation.[12,13] RNase T2 cleaves single-stranded RNA (ssRNA) with a preference for purine-uridine motifs, thereby generating fragments that are terminated with a purine 2′,3′-cyclic phosphate and initiated with a 5′ hydroxyl uridine. Thereby, RNase T2 activity contributes to two critical steps: on the one hand, RNase T2 generates purine 2′,3′-cyclic phosphate-terminated fragments that engage pocket 2 and on the other hand it results in the increase of

uridine, while the latter mechanism is not fully explored. Interestingly, loss-of-function studies have shown that RNase T2 also plays a role upstream of TLR7.[14] However, despite its genetically proven involvement, the precise mechanistic role of RNase T2 in relation to TLR7 remains unclear, which prompted the initiation of this study.

RESULTS

RNase T2 is required for TLR7 activation

To study TLR7 signaling in a physiologically relevant setting, we used the CAL-1 cell line, a human pDC line derived from a male patient with a blastic plasmacytoid DC neoplasm.[15] CAL-1 cells express a similar repertoire of PRRs as primary pDCs, in particular TLR7 and TLR9, and respond to ssRNA and CpG DNA with the production of antiviral and pro-inflammatory cytokines. We stimulated wild-type (WT) or *TLR7*$^{-/y}$ CAL-1 cells with the RNA-based TLR7 agonists RNA40[2] and RNA9.2s.[16] RNA40 was delivered as a phosphodiester version (RNA40^{O}) as well as a stabilized phosphorothioate version (RNA40^{S}) (Figures 1A and 1B). The small molecule TLR7 agonists, R848 and 2′,3′-cGMP, and CpG DNA—either phosphodiester (CpG^{O}) or phosphorothioate (PTO)-stabilized (CpG^{S}) engaging TLR9—were used as controls. The ORNs triggered a robust type I interferon (IFN) response, albeit at a lower magnitude compared with R848, 2′,3′-cGMP, and CpG DNA (Figure 1A). At the concentration tested, the phosphorothioate-stabilized version RNA40^{S} was completely inactive in CAL-1 cells. As expected, ablation of TLR7 resulted in a complete loss of cytokine production for ORNs as well as for the small molecule TLR7 agonists. CpG DNA triggered IFN responses in both WT and TLR7-deficient CAL-1 cells, yet only when the phosphorothioate-stabilized ODNs were used (Figure 1A). Similar results were obtained in primary pDCs that responded to phosphodiester RNA40 as well as RNA9.2s, but not to the phosphorothioate-stabilized version of RNA40. R848 and 2′,3′-cGMP also triggered TLR7 activation, with R848 being a more potent activator compared with 2′,3′-cGMP (Figure 1C). Addressing the role of RNase T2 in this context revealed that the ORNs were indeed completely dependent on this enzyme for their immune-stimulatory activity, while its requirement could be bypassed by using R848 or 2′,3′-cGMP as direct pocket 1 agonists (Figure 1D). In light of the notion that RNase T2 generates 2′,3′-cGMP-terminated RNAs and the fact that 2′,3′-cGMP levels are strongly decreased in *RNASET2*$^{-/-}$ cells (Greulich et al.[12] and below), we addressed whether RNase T2 could liberate 2′,3′-cGMP from ssRNA *in vitro*. To address this, we designed an ORN in which an RNase T2 cleavage site (GU) was positioned directly at the 5′ end, while we also generated ORNs in which this dinucleotide motif was stepwise moved to the 3′ end of the ORN (Figure 1E). Testing these ORNs using recombinant RNase T2 revealed that RNase T2 required at least two nucleotides 5′ to its recognition motif to cleave. These results suggested that RNase T2 on its own was not able to release 2′,3′-cGMP within the endolysosomal compartment, but rather additional enzyme activities were required for this.

A role for PLD exonuclease activity upstream of TLR7

Because RNase T2 was unable to release the TLR7 first binding pocket ligand by itself, we therefore turned our attention to possible exonucleases of the secretory pathway. Here, phospholipase 3 and 4 (PLD3 and PLD4) operate within the lysosomal compartment.[17,18] Mining publicly available bulk (Figure 2A) and single-cell RNA sequencing (RNA-seq) datasets (Figure 2B) indicated that PLD3 was broadly expressed in myeloid cells, whereas PLD4 was largely confined to pDCs. In the absence of suitable antibodies to detect PLD3 or PLD4 protein expression at the endogenous level, we used quantitative mass spectrometry to study the expression of PLD3 and PLD4 in CAL-1 cells, pDCs, and CD14^{+} monocytes. Both enzymes were detected, yet PLD4 was far more abundant than PLD3 in both pDCs and CAL-1 cells. As such, PLD4 levels exceeded PLD3 levels in primary pDC by 78-fold and about 20-fold in CAL-1 cells. Monocytes, on the other hand, displayed intermediate expression levels for both enzymes (Figure 2C). Ablating PLD3 and PLD4 revealed that CAL-1 cells deficient for both enzymes displayed a completely blunted response toward RNA oligonucleotides, similar to RNase T2-deficient cells. Conversely, CpG-DNA-mediated activation of CAL-1 cells was dramatically enhanced for phosphodiester DNA,[17] while backbone-stabilized PTO ODNs even showed a reduced response in these cells (Figure 2D). When we studied CAL-1 cells deficient in either PLD3 or PLD4, we observed that PLD3 deficiency on its own dramatically boosted responses toward phosphodiester CpG DNA, while this was not observed when knocking out PLD4 (Figure S1A). On the other hand, *PLD4*$^{-/-}$ cell clones showed a greatly blunted RNA response yet showed the same low response toward CpG DNA as WT cells. These results suggest that PLD3 primarily degraded DNA, thereby preventing TLR9 activation, whereas PLD4-mediated degradation of RNA played a positive regulatory role upstream of TLR7. However, screening a larger panel of several PLD4-deficient clones also recovered some *PLD4*$^{-/-}$ CAL-1 cells that were still responding to ssRNA (Figure S1A). In light of the reported redundancy of PLD3 and PLD4 processing DNA and RNA ([17,18] and see below), we ascribe the phenotype in these *PLD4*$^{-/-}$ cell clones to a compensatory increase in PLD3 activity. Indeed, reconstituting *PLD3*$^{-/-}$ × *PLD4*$^{-/-}$ cells with PLD3 (Figure S1B) partially recovered the RNA response, indicating that PLD3 can compensate for the pro-TLR7 activity in the absence of PLD4 (Figure S1C). To avoid such redundancies, we therefore conducted all subsequent experiments addressing the functional relevance of PLD3 and PLD4 in *PLD3*$^{-/-}$ × *PLD4*$^{-/-}$ CAL-1 cells.

To further corroborate the role of PLDs upstream of TLR7, we additionally ablated PLD3 or PLD3 and PLD4 in primary human monocytes using CRISPR/Cas ribonucleoprotein particles and differentiated these cells into macrophages. After 8 days, we stimulated those cells with ssRNA40^{O} in the presence of the selective TLR8 inhibitor CU-CPT9a[21] to monitor solely TLR7 activation. R848 and lipopolysaccharide (LPS) were further used as controls. Like in CAL-1 cells, we observed a largely blunted TLR7 response in the absence of PLD3 and PLD4 upon stimulation with ssRNA. Lack of PLD3 alone already attenuated TLR7 activation in these primary macrophages, indicating that PLD3 constitutes the functionally predominant PLD exonuclease in these cells (Figure 2E). Lastly, we made use of the myeloid cell line BLaER1, which is similar to primary human

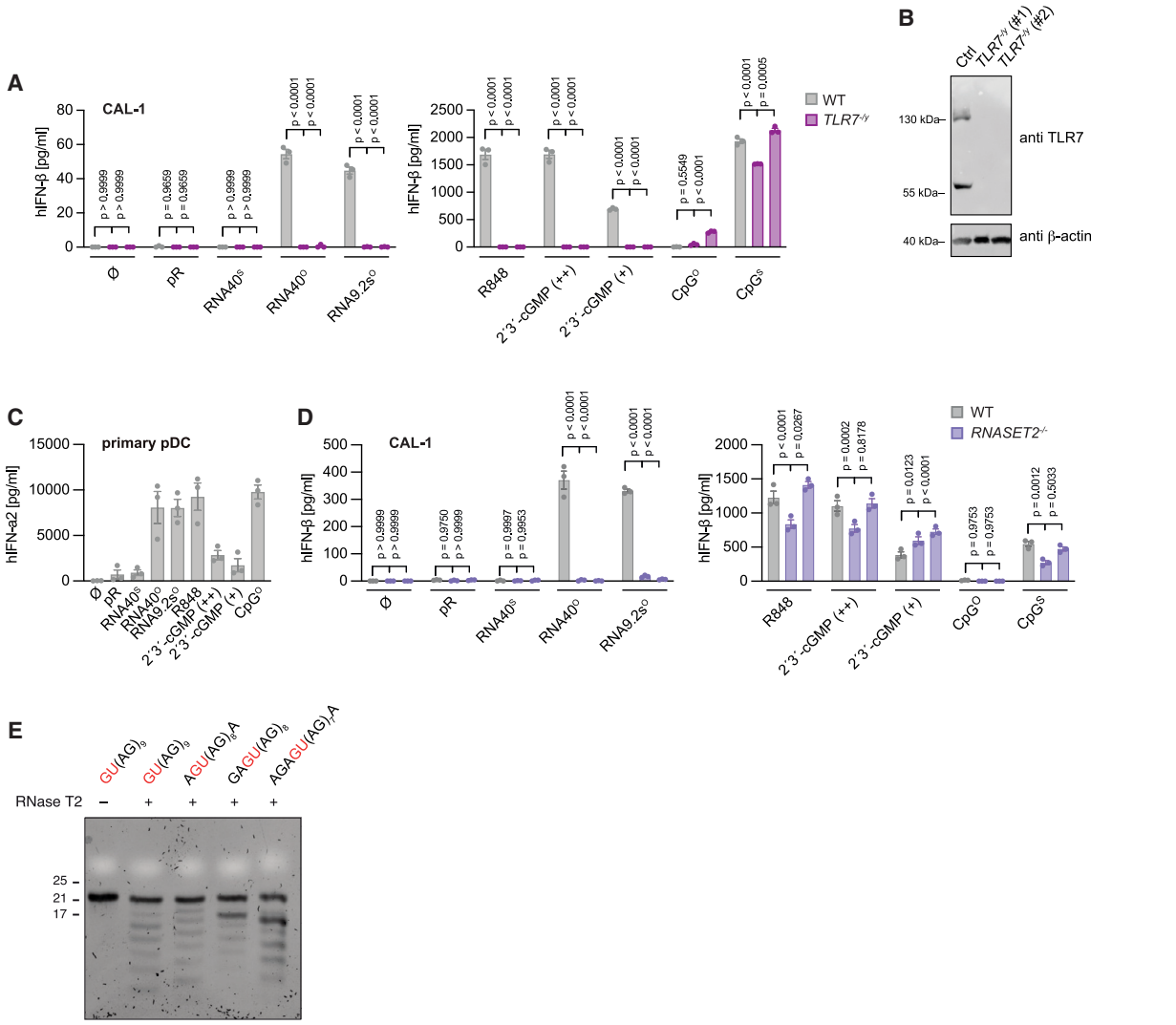

Figure 1. RNase T2 acts upstream of TLR7

(A) Unmodified CAL-1 cells (WT) or two independent *TLR7*$^{-/y}$ CAL-1 clones were unstimulated or stimulated with pR, RNA40^{S}, RNA40^{O}, RNA9.2s^{O}, R848, 2′,3′-cGMP (++ = 1 mM, + = 0.5 mM), CpG^{O}, or CpG^{S}. After 16 h, IFN-β release was measured by enzyme-linked immunosorbent assay (ELISA). Data are depicted as mean ± SEM of *n* = 3 independent experiments. Statistical analysis was conducted by two-way ANOVA with Dunnett's multiple comparison tests.

(B) TLR7 expression in CAL-1 WT and *TLR7*$^{-/y}$ CAL-1 clones by immunoblot. One representative blot of three independent experiments is shown.

(C) Isolated primary plasmacytoid dendritic cells were unstimulated or stimulated with pR, RNA40^{S}, RNA40^{O}, RNA9.2s^{O}, R848, 2′,3′-cGMP (++ = 1 mM, + = 0.5 mM), and CpG^{O}. After 24 h, IFN-α2 release was measured by ELISA. Data are depicted as mean ± SEM of *n* = 3 independent donors.

(D) Unmodified CAL-1 cells (WT) or two independent *RNASET2*$^{-/-}$ CAL-1 clones were stimulated as in (A) and IFN-β release was measured. Data are depicted as mean ± SEM of *n* = 3 independent experiments. Statistical analysis was conducted by two-way ANOVA with Dunnett's multiple comparison tests.

(E) Urea gel of indicated substrates digested with RNase T2 (0.37 nM). One representative gel of three independent experiments is shown.

monocytes functional for both TLR7 and TLR8.[12] BLaER1 cells responded to phosphodiester ORNs with a mixed TLR7 and TLR8 response, with the TLR7 component being more pronounced at high ORN concentrations (Figure S1D). In the absence of TLR8, the TLR7 response triggered by ORNs was completely dependent on PLD3 and PLD4, mirroring the results obtained with CAL-1 cells and primary human macrophages (Figure S1E). Altogether, these results indicated that PLD exonuclease activity negatively regulated the recognition of CpG DNA via TLR9, while it was critically required to process RNA for it to exert TLR7 agonism.

PLD3 and 4 liberate the pocket 1 ligand guanosine 2′,3′-cyclic monophosphate from RNase T2-digested RNA

PLD3 and PLD4 exert 5′ exonuclease activity and primarily release 3′monophosphate nucleosides from their substrates.[17,18] We expressed and purified PLD3 and PLD4 (Figure S2A) and studied their nucleolytic activity toward phosphodiester RNA oligonucleotide substrates that exert a fluorescent signal upon exonucleolytic degradation of the 5′ terminus.[22] In line with previous reports, we found that PLD3 exerted far higher catalytic activity toward RNA (Figures 3A and 3B). As such, the

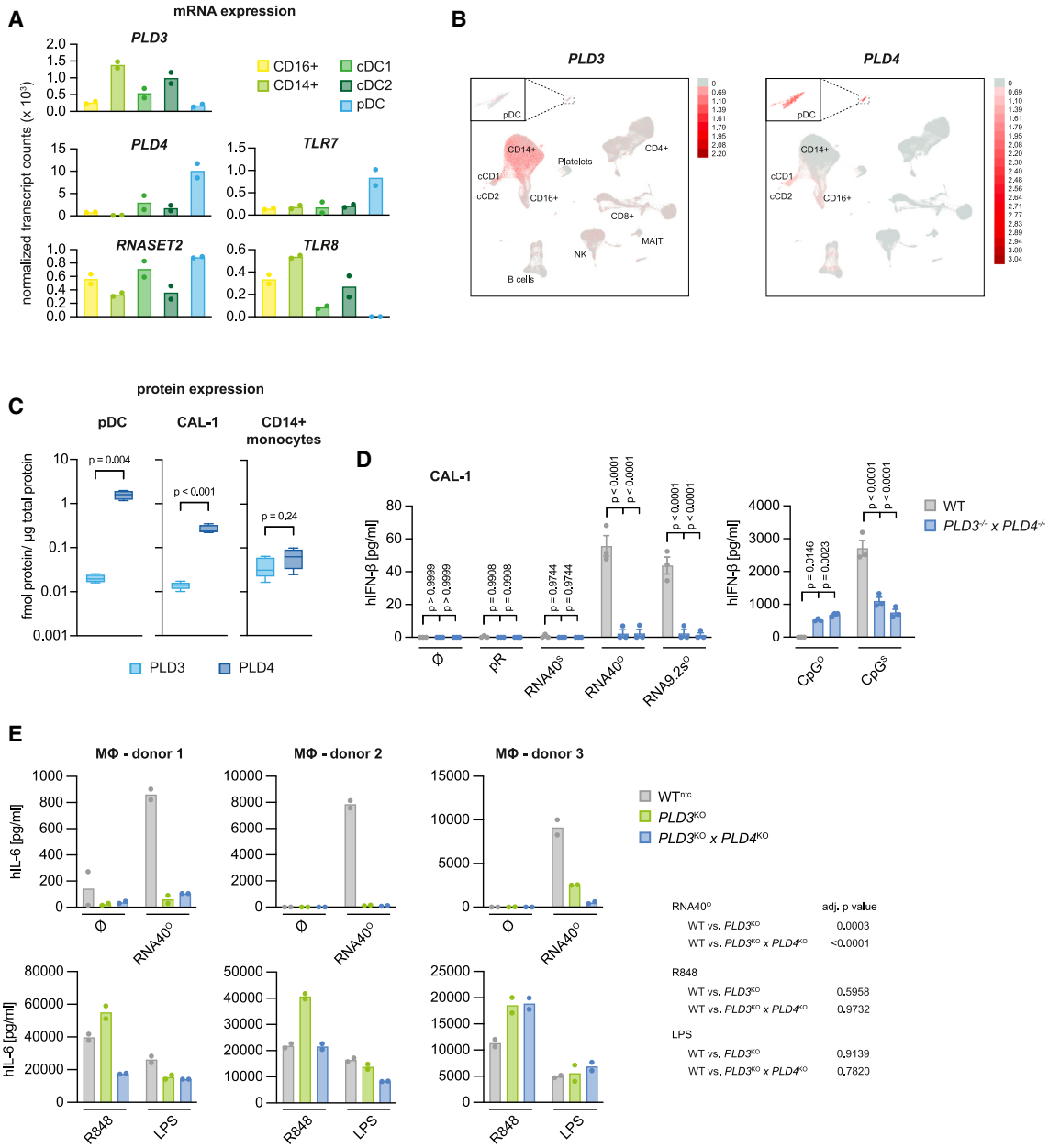

Figure 2. PLD3 and PLD4 act upstream of TLR7

(A) mRNA expression levels of PLD3, PLD4, RNase T2, TLR7, and TLR8 in indicated cell types are plotted.

(B) Single-cell RNA-seq data of human PBMCs from Hao et al.[19] were visualized using the UCSC Cell Browser[20] for the transcripts PLD3 and PLD4. Color coding represents the range of gene expression. The insert in the upper left corner specifically highlights the pDC population. Annotations for relevant cell populations were retrieved as annotated.

(C) Quantification of PLD3 and PLD4 protein expression in CAL-1 cells, primary plasmacytoid dendritic cells, and primary monocytes. Data are presented as box and whiskers of n = 4–5 independent experiments, statistics indicate a paired two-tailed Student's t test.

(D) Unmodified CAL-1 cells (WT) or two independent *PLD3*$^{-/-}$ × *PLD4*$^{-/-}$ CAL-1 clones were unstimulated or stimulated with pR, RNA40^{S}, RNA40^{O}, RNA9.2s^{O}, CpG^{O}, or CpG^{S}. After 16 h, IFN-β release was measured by ELISA. Data are depicted as mean ± SEM of n = 3 independent experiments. Statistical analysis was conducted by two-way ANOVA with Dunnett's multiple comparison tests.

(E) Indicated knockouts of primary human monocytes were unstimulated or stimulated with ssRNA40^{O} in the presence of CU-CPT9a, R848, and LPS. After 16 h, IL-6 release was measured by ELISA. Each replicate of 3 independent donors is depicted. For statistical analysis, the data of each donor was normalized to WT^{NTC} and two-way ANOVA was conducted on log-transformed data with Dunnett's multiple comparison test.

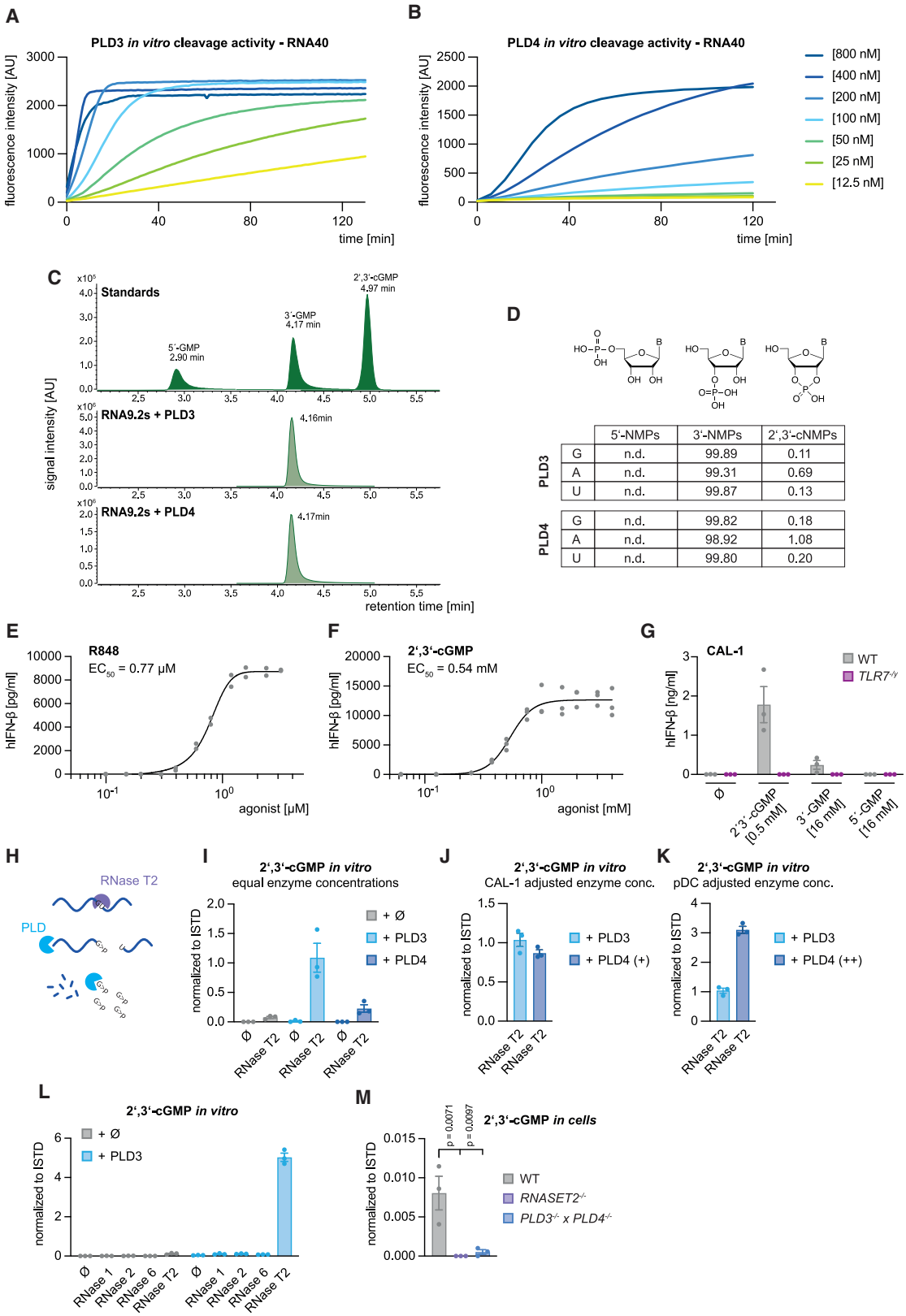

(legend on next page)

calculated specific activity of PLD3 exceeded PLD4 by approximately 17-fold under these conditions. Analyzing RNA degradation at different enzyme concentrations using gel electrophoresis corroborated the notion of PLD3 being more processive than PLD4 (Figures S2B and S2C). Moreover, PLD3 was also far more processive toward a DNA substrate compared with PLD4 (Figure S2D).[17] Studying PLD3 and PLD4 RNA cleavage products using mass spectrometry, we found that both PLD3 and PLD4 released 3′- nucleoside monophosphates (NMPs),[17] while only trace amounts of 2′,3′-cNMP were detected (e.g., for 2′,3′-cGMP 0.1%–0,2% of all guanosines) (Figures 3C, 3D, and S2E). On the other hand, 5′-NMPs were not found at all. Comparing the potency of different guanine nucleotides however revealed that only 2′,3′-cGMP exerted potent TLR7 activation (effective concentration [EC_{50}] = 0.54 mM) with a similar efficacy as R848 (Figures 3E and 3F). 3′-GMP at concentrations 32× higher than the EC_{50} of 2′,3′-cGMP were needed to exert a measurable response, while 5′-GMP was completely inactive in CAL-1 cells (Figure 3G). Similar results were obtained from isolated primary pDCs, showing a robust TLR7 response induced by 2′,3′-cGMP, while 3′-GMP elicited weaker activation and 5′-GMP failed to induce TLR7 activation at all (Figure S2F). Together, these results suggest that 2′,3′-cGMP constitutes the natural pocket 1 ligand for TLR7 and that PLD exonuclease activity toward RNA substrates was not sufficient to generate this agonist. Given the substrate specificity of RNase T2 generating purine 2′,3′-cyclic phosphate-terminated fragments, we hypothesized that the combined activity of PLD exonuclease activity and RNase T2 endonuclease activity might be required for the production of 2′,3′-cGMP (Figure 3H). To address this possibility, we studied the production of 2′,3′-cGMP when processing RNA with PLD3 or PLD4 alone and with or without RNase T2 *in vitro*. Only the combination of PLD3 or PLD4 and RNase T2, but not the single enzymes, were able to generate substantial amounts of 2′,3′-cGMP when processing an ssRNA molecule (Figure 3I). At the same PLD enzyme concentrations, PLD3 released greater levels of 2′,3′-cGMP from ssRNA *in vitro* due to its stronger catalytic activity (Figure 3I). However, we found that PLD4 protein levels exceed those of PLD3 in primary pDCs by 78-fold and by 20-fold in CAL-1 cells (Figure 2C). Therefore, studying 2′,3′-cGMP release under adjusted enzyme concentrations using a 20-fold lower concentration of PLD3 revealed a comparable release of the nucleotide by PLD3 and PLD4, suggesting that both proteins equally contribute to the release of 2′,3′-cGMP in CAL-1 cells (Figure 3J). However, at a concentration 78-fold higher than that of PLD3, mimicking the condition in primary pDCs, PLD4 produced greater levels of 2′,3′-cGMP *in vitro*, implying that PLD4 serves as the main enzyme producing 2′,3′-cGMP in conjunction with RNase T2 in primary pDCs (Figure 3K). We also used recombinantly expressed RNase 1, RNase 2, and RNase 6—RNase A family endonucleases known to cleave after pyrimidines—as controls (Figure 3L). However, none of these enzymes were able to release nearly as much 2′,3′-cGMP as RNase T2 when combined with PLD3. In line with this notion, cells deficient in either RNase T2 or PLD3 and PLD4 displayed absent or strongly reduced 2′,3′-cGMP levels when stimulated with ssRNA (Figure 3M). Altogether, these results showed that PLD activity together with RNase T2 was required to generate the pocket 1 ligand 2′,3′-cGMP for TLR7.

PLD exonucleases are required for pocket 2 ligands

We hypothesized that *PLD3*$^{-/-}$ × *PLD4*$^{-/-}$ cells could be rescued with 2′,3′-cGMP, as it was the case for *RNASET2*$^{-/-}$ cells (Figure 1D). However, when treating *PLD3*$^{-/-}$ × *PLD4*$^{-/-}$ cells with 2′,3′-cGMP, we observed a complete lack of an immune response. R848 also exerted diminished activity in CAL-1 monoclones, CAL-1 *PLD3*^{KO} × *PLD4*^{KO} pool knockout cells, and BLaER1 monocytes (Figures 4A, S3A, and S3B). We also investigated the impact of PLD deficiency on tumor necrosis factor alpha (TNF-α) and interleukin-6 (IL-6) release after stimulation of *PLD3*$^{-/-}$ × *PLD4*$^{-/-}$ monoclones. Similar to the effects seen for IFN-β release, we observed blunted responses upon transfection of ssRNA and upon stimulation with 2′,3′-cGMP. Also, R848 displayed reduced activity in *PLD3*$^{-/-}$ × *PLD4*$^{-/-}$ clones, yet only when using concentrations near or below its EC_{50} value (Figures S3C and S3D). We further generated J774 mouse macrophages lacking PLD3. In line with previous work, we observed diminished TLR7 responses upon stimulation with ssRNA40 (Figure S3E). Stimulation of those cells with

Figure 3. RNase T2 and PLD enzymes release 2′,3′-cyclic GMP

(A and B) Fluorescence intensity signal of FAM-RNA40-BMN-Q530 over time, incubated with indicated concentrations of (A) PLD3 or (B) PLD4. Data are depicted as mean of $n = 3$ independent experiments.

(C) Overlay of extracted ion chromatograms (EIC) of 5′-GMP, 3′-GMP, and 2′,3′-cyclic GMP. Top: standards used as reference. Middle: *in vitro* digests of RNA9.2s with PLD3 (250 nM). Bottom: PLD4 (250 nM).

(D) Normalized signal areas of EIC from released 5′-NMPs, 3′-NMPs, and 2′,3′-cNMPs by PLD3 (250 nM) and PLD4 (250 nM) after degradation of $RNA9.2s^{O}$ in %.

(E and F) CAL-1 WT cells (300,000 cells/well) were stimulated with increasing concentrations of R848 and 2′,3′-cGMP. After 16 h, IFN-β release was determined by ELISA. Each replicate of $n = 2$ (E) or $n = 3$ (F) independent experiments is depicted. A four-parameter dose-response curve was fitted to calculate half-maximal effective concentration (EC_{50}).

(G) CAL-1 cells (300,000 cells/well) of indicated genotypes were unstimulated or stimulated with indicated concentrations of 2′,3′-cGMP and 3′-GMP. Data are depicted as mean ± SEM of three independent experiments.

(H) Schematic view of the *in vitro* digestion assay.

(I) $RNA40^{O}$ was digested with RNase T2 (370 nM), PLD3 (250 nM), and PLD4 (250 nM) or in combinations of RNase T2 (370 nM) with either PLD3 (250 nM) or PLD4 (250 nM) for 20 min, and the release of 2′,3′-cGMP was analyzed by LC-MS.

(J and K) $RNA40^{O}$ was digested with RNase T2 (370 nM) in combination with either PLD3 (+ = 2.5 nM), PLD4 (+ = 50 nM), or with PLD4 (++ = 195 nM) for 20 min, and the release of 2′,3′-cGMP was analyzed by LC-MS.

(L) $RNA40^{O}$ was digested with RNase 1 (5.7 nM), RNase 2 (27 nM), RNase 6 (29 nM), or RNase T2 (37 nM) only or in combination with PLD3 (25 nM) for 30 min, and the release of 2′,3′-cGMP was analyzed by LC-MS. For (I), (J), (K), and (L), data are depicted as mean ± SEM of $n = 3$ independent experiments.

(M) Detection of 2′,3′-cGMP in cell lysates of $RNA40^{O}$-stimulated WT, RNase T2, or *PLD3*$^{-/-}$ × *PLD4*$^{-/-}$ CAL-1 cells by LC-HRMS. Data are depicted as mean ± SEM of $n = 3$ independent experiments. Statistical analysis was conducted by one-way ANOVA with Dunnett's multiple comparison tests.

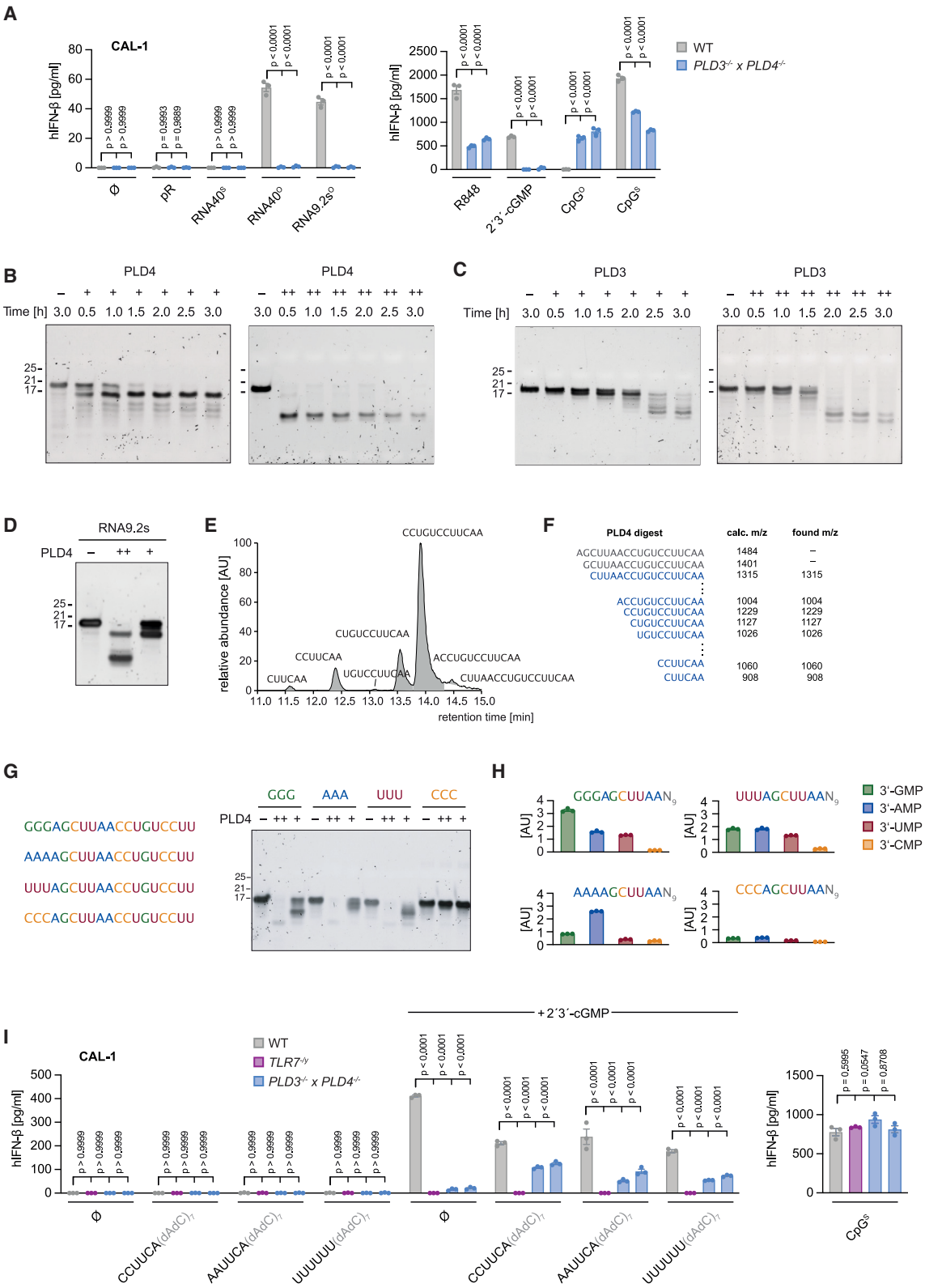

Figure 4. PLD enzymes create TLR7 second binding pocket fragments

(A) CAL-1 cells of indicated genotypes were unstimulated or stimulated with pR, RNA40^{S}, RNA40^{O}, RNA9.2s^{O}, R848, 2′,3′-cGMP (0.5 mM), CpG^{O}, and CpG^{S}. After 16 h, IFN-β release was determined by enzyme-linked immunosorbent assay (ELISA). Data are presented as mean ± SEM of $n = 3$ independent experiments.

(legend continued on next page)

R837 also revealed reduced TLR7 responses when concentrations close to its EC_{50} value were used (EC_{50} = 2.45 μM) (Figures S3E and S3F), mirroring the pattern observed for IL-6 and TNF release in CAL-1 cells. Assessing the whole proteome of *PLD3*$^{-/-}$ × *PLD4*$^{-/-}$ CAL-1 cells excluded the possibility that combined PLD3 and PLD4 deficiency resulted in the secondary perturbation of the proteome, thus potentially affecting TLR7 activity (e.g., lysosomal proteins) (Table S1). Consequently, these results suggested that PLD activity was not only required to generate 2′,3′-cGMP in conjunction with RNase T2 but was also involved in generating ligands to engage the second binding pocket. However, this posed a conundrum, as complete exonucleolytic decay of lysosomal RNA by PLDs should yield mononucleotides, not fragments large enough to occupy the second binding pocket. When we studied RNA degradation by PLD4 at two different enzyme concentrations over a period of 180 min, PLD4 displayed a distinct fragment patterning, indicative of these enzymes "stalling" at certain sites of their substrates (Figure 4B). Similar results were obtained for PLD3 under limiting-enzyme concentrations (Figure 4C). LC-HRMS analysis of PLD4-processed RNA9.2s revealed that largely cytidine-initiated fragments were generated, suggesting that PLD4 preferably disengaged with its substrate when a 5′-C was reached (Figures 4D–4F). To further characterize this phenomenon, we designed substrates with either three consecutive cytidines, uridines, adenosines, or guanosines and subjected these to PLD4 processing. Assessing cleavage of these ORNs indicated that PLD4 showed a preference for degrading substrates that initiated with U, followed by those starting with G and A, with C-initiated substrates being degraded least efficiently (U>G>A>>C) (Figure 4G). LC-HRMS analysis of PLD4-processed RNA oligonucleotides corroborated these findings, with 5′-C substrates being processed poorly (Figure 4H). Altogether, these results suggest that PLD4 and PLD3 may indeed exert differential activity on different types of RNA fragments, sparing certain fragments from exonucleolytic degradation.

We hypothesized that this selective degradation could lead to the accumulation of ORN fragments as potential pocket 2 ligands within the lysosomal compartment. We therefore investigated whether we could bypass the TLR7 activation defect in *PLD3*$^{-/-}$ × *PLD4*$^{-/-}$ cells by co-delivering 2′,3′-cGMP and short ORN fragments. We designed different 6-mer ORN molecules attached to the 5′ end of a 14-mer deoxy oligonucleotide to ensure efficient lysosomal delivery[12] and transfected these oligos into WT, *TLR7*$^{-/y}$, or *PLD3*$^{-/-}$ × *PLD4*$^{-/-}$ cells (Figure 4I). These oligos alone failed to induce immune responses in any of these cell types. However, when delivered together with 2′,3′-cGMP, they induced a measurable immune response in WT cells and this was also observed in *PLD3*$^{-/-}$ × *PLD4*$^{-/-}$ cells. 2′,3′-cGMP, on the other hand, was completely inactive in *PLD3*$^{-/-}$ × *PLD4*$^{-/-}$ cells, while being a potent agonist in WT cells. Collectively, these results indicate that PLDs are not only required to generate pocket 1 ligands in conjunction with RNase T2 but that they also process RNA into fragments suitable for ligand-binding pocket 2, a function for which RNase T2 is not required.

PLD3 and PLD4 form a dimer that forms 2 substrate binding pockets

To obtain a better mechanistic understanding of how exonucleolytic PLDs process nucleic acids, we used cryoelectron microscopy (cryo-EM) to obtain a structural model of the soluble catalytic domain of human PLD3. We mainly focused on PLD3 due to its better expression and purification characteristics. During size exclusion chromatography (SEC) we noted that PLD3 forms a stable dimer (Figure 5A), which was also substantiated by mass photometry analysis (Figure 5B). Analogous results were obtained when expressing PLD4 (Figures 5A and 5B). We recorded datasets of PLD3 as well as PLD3 in complex with ssRNA. Two-dimensional (2D) classifications of the apoenzyme data yielded C2 symmetric dimeric PLD3 classes. Three-dimensional (3D) reconstruction of the dimer using C2 symmetry resulted in a map with a global resolution of 2.87 Å, allowing model building of residues 79–490 (Figures 5C and S4). Although PLD3 is a member of the phospholipase family with two HxKxxxxD/E motifs resulting from internal duplication, it also dimerizes. This dimerization leads to the formation of two active sites on opposite sides of the dimer (Figure 5C). A structural superposition with the catalytic domain of human PLD1 (PDB: 6U8Z[23]) indicated that the typical bi-lobal fold is retained in each protomer and that the conformation of lobe 1 as well as the typical β-sheets are mostly similar (Figure S5A). Conversely, lobe 2 of hPLD1 shows significant structural differences and large insertions (Figure S5B). However, the arrangement of the enzymatically critical HxK motif residues H201 and K203, as well as H416 and K418 in PLD3, are identical to PLD1 and other PLD family members (Figure S5C). This suggests that PLD3 cleaves the single-stranded DNA (ssDNA)/ssRNA substrates utilizing a similar two-step mechanism, as seen by other DNases of the PLD superfamily, by forming a phospho-histidine intermediate.[24] Most likely histidine 416 acts in the reaction as the nucleophile activated by Glu 229, whereas histidine 201 serves as a general acid to protonate

Statistical analysis was conducted by two-way ANOVA with Dunnett's multiple comparison tests. Note that the WT data are identical with the ones shown in Figure 1A.

(B) Urea gels of RNA9.2s^{O} digested with PLD4 (+ = 25 nM, ++ = 250 nM) over time. One representative gel of three independent experiments is shown.

(C) Urea gels of RNA9.2s^{O} digested with PLD3 (+ = 0.39 nM, ++ = 1.56 nM) over time. One representative gel of two independent experiments is shown.

(D) Urea gel of RNA9.2s^{O} (1 μg) incubated with PLD4 (++ = 250 nM, + = 25 nM) for 2 h. One out of three independent experiments is shown.

(E) LC-HRMS total ion current (TIC) chromatogram of RNA9.2s^{O}-derived ORN fragments after digestion with PLD4 (250 nM) for 2 h.

(F) Calculated and found masses (*m/z*) of RNA9.2s-derived ORN fragments after digestion with PLD4 (250 nM) for 2 h.

(G) Urea gel of indicated substrates digested with PLD4 (++ = 250 nM, + =25 nM). One out of two independent experiments is shown.

(H) LC-MS/MS analysis of depicted substrates digested with PLD4 (250 nM) for 20 min. Data were normalized to the amount of the different nucleosides present in the sequence and are depicted as mean ± SEM of *n* = 3 independent experiments.

(I) CAL-1 cells of indicated genotypes were unstimulated or stimulated with 2′,3′-cGMP (0.5 mM), short ORNs, or ORNs in combination with 2′,3′-cGMP (0.5 mM). Data are depicted as mean + SEM of *n* = 3 independent experiments. Statistical analysis was conducted by two-way ANOVA (left panel) or one-way ANOVA (right panel) with Dunnett's multiple comparison tests.

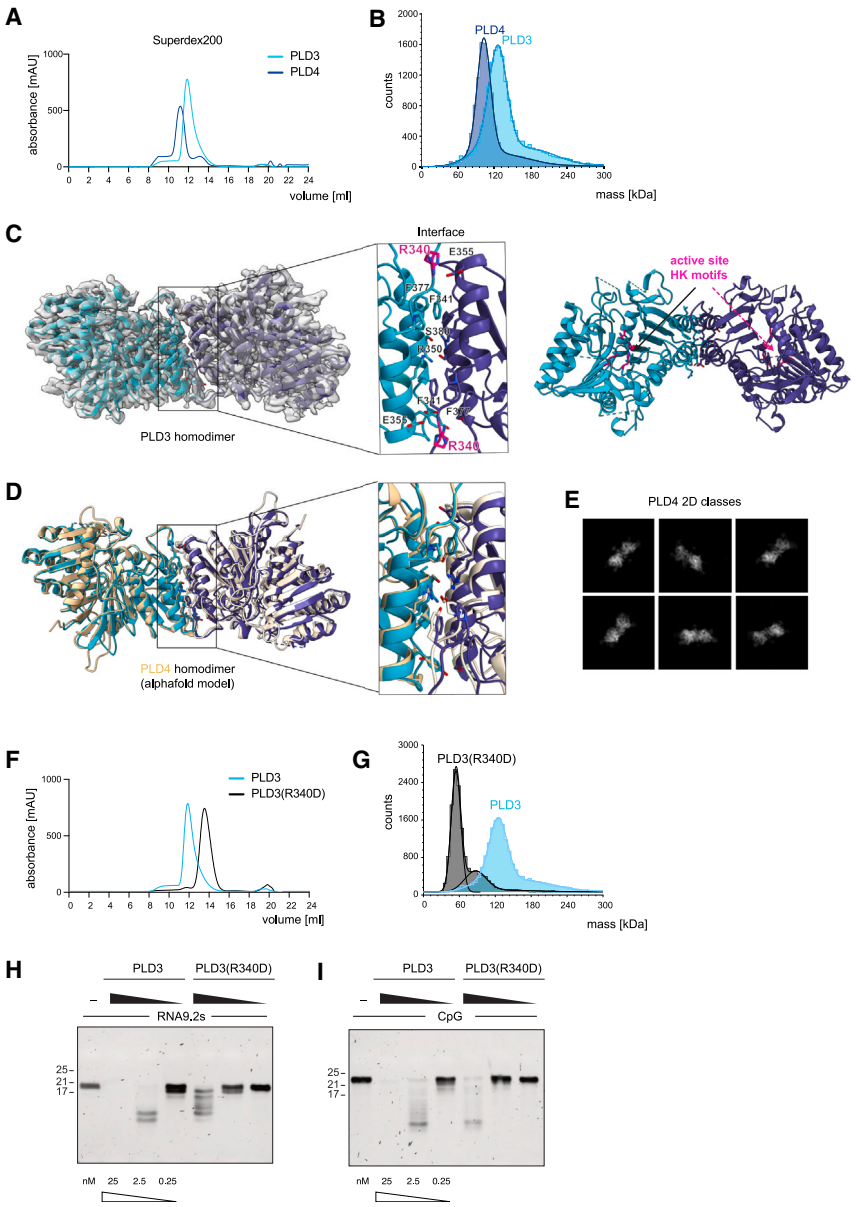

Figure 5. PLD3 and PLD4 form homodimers

(A) Size exclusion chromatography (SEC) run of PLD3 superimposed with the SEC run of PLD4.

(B) Mass distribution of PLD3 and PLD4 observed by mass photometry.

(C) Ribbon representation of the PLD3 dimer shown together with the cryo-EM density map. The inset shows a detailed view of the dimer interface, with the involved residues shown in stick representations. The mutated residue R340 and active site HxK motifs are highlighted in pink.

(D) Structural comparison between the PLD3 cryo-EM structure, colored in turquoise and dark blue, and the PLD4 model predicted by Alphafold, colored in beige. The inset illustrates the comparison of the PLD3/PLD4 dimer interface, with involved residues highlighted using stick representations.

(E) Representative 2D classes of PLD4 particles illustrating the dimeric conformation.

(F) Size exclusion chromatography (SEC) run of PLD3 superimposed with the SEC run of PLD3(R340D). Note that the SEC control run of PLD3 is identical to Figure 5A.

(G) Mass distribution of PLD3 and PLD3(R340D) observed by mass photometry. Note that the mass distribution control of PLD3 is identical to Figure 5B.

(H and I) Urea gels of RNA9.2s^{O} and CpG^{O}-DNA digested with indicated concentrations of PLD3 and PLD3(R340D). One out of two independent experiments is shown.

the oxygen atom of the leaving group.[25] The two adjacent lysine residues, which have been shown to be involved in the coordination of the substrate, extend their ε-amino group into the catalytic center. All four residues are located buried in a cleft formed by mainly hydrophobic and positively charged residues. Apart from the four active site residues, the substrate binding cleft largely differs from human PLD1, which is in agreement with the different substrate types cleaved (Figure S5B). The two PLD3 protomers assemble into a dimer with C2 symmetry, while the dimer interface is formed by hydrophobic interactions (residues F341, F377, and L384)—a salt bridge between residues R340 and E355—as well as hydrogen bonds between R350 and S380, and Y354 and S373, respectively (Figure 5C). A comparison with a PLD4 dimer model calculated by Alphafold[26] suggested that the dimer interface is largely conserved in PLD4 (Figure 5D). To confirm the dimeric PLD4 conformation, a cryo-EM dataset was collected, yielding 2D classes with a structure similar to the PLD3 dimer (Figure 5E). However, the preferred orientation of the particles hindered the reconstruction of a 3D structure.

To prove the structurally determined interface and to analyze the importance of dimerization for the nucleolytic activity of PLD3, we introduced a charge reversal mutation at residue R340 (R340D), thereby preventing the formation of the polar interaction to E355 of the second protomer. The mutant PLD3^{R340D} eluted as a monomer from the size exclusion column and exhibited monomeric behavior in the mass photometry analysis (Figures 5F and 5G). The exonucleolytic activity of the R340D mutant was significantly reduced when using ssRNA9.2s and CpG ssDNA as substrates (Figures 5H and 5I). Because residue R340 is far from the active site HxK motif, we concluded that the dimeric state of PLD3 is important for substrate recognition. PLD3 mutations are linked to susceptibility to Alzheimer's disease[27] (PLD3^{V232M}) and to spinocerebellar ataxia[28] (PLD3^{L308P}), although their exact role in these diseases is not yet understood. Neither V232 nor L308 are localized in close proximity to the catalytic center or to the dimerization interface (Figure S5D). V232 is located in the hydrophobic core of PLD3, and its mutation to methionine might influence the correct folding of PLD3. On the other hand, L308 is situated in a helix that is in the vicinity of the dimer interface. Therefore, a mutation to proline could interrupt the helix formation and influence the folding in this area,

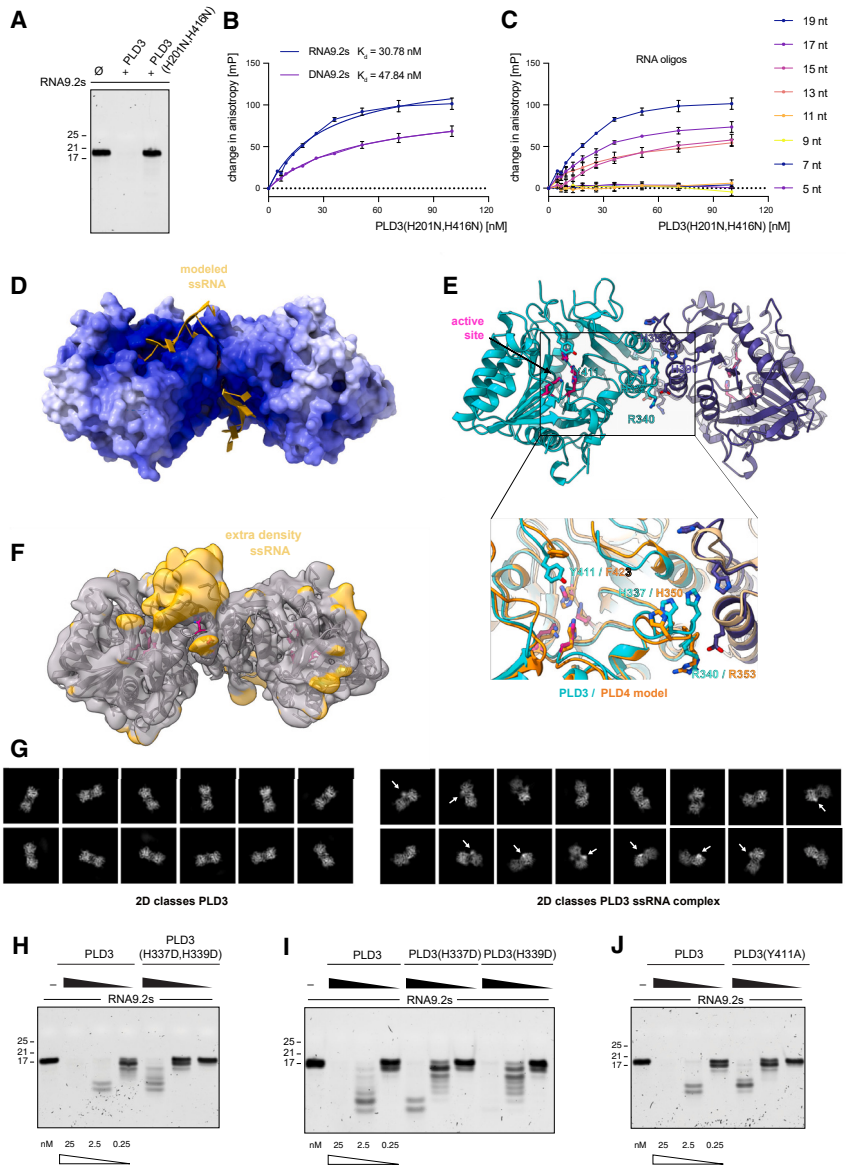

Figure 6. PLD3 shows high-affinity binding to long oligonucleotides

(A) Urea gel of RNA9.2s^{O} incubated with PLD3 (250 nM) and PLD3(H201N, H416N) (250 nM). One out of three independent experiments is shown.

(B and C) Fluorescence anisotropy assays assessing the binding of PLD3(H201N, H416N) at increasing concentrations to indicated substrates. Data are shown as mean ± SEM of n = 3 independent experiments. Note that the 19-nt RNA9.2s binding data are identical in (B) and (C).

(D) The electrostatic surface of the PLD3 dimer, calculated with APBS at pH 5, illustrates the presence of two positively charged areas. The two ssRNA segments, colored in gold, have been modeled using Hdock.

(E) Ribbon representation of PLD3 with highlighted active site HxK motif colored in pink and residues presumably involved in substrate recognition shown as sticks and color coded according to the corresponding protomer, with turquoise or dark blue, respectively. The inset shows a detailed view of the comparison between PLD3 (turquoise) and PLD4 (orange) at the active site cleft, illustrating the conservation of the highlighted residues.

(F) Cryo-EM density map for PLD3 bound to ssRNA highlighting the additional density appearing in gold.

(G) Representative 2D classes of PLD3 particles or PLD3 ssRNA complex particles.

(H–J) Urea gels of RNA9.2s^{O} digested with decreasing concentrations of PLD3 or with decreasing concentrations of depicted PLD3 mutants. For all urea gels, one out of two independent experiments is shown.

including the dimer interface. Expression of these mutants showed that PLD3^{V232M} had, in part, lost its capacity to form a dimer, while it appeared to form multimers in SEC, whereas PLD3^{L308P} was fully monomeric (Figures S5E–SH). Consistent with the relevance of dimer formation, the catalytic activity of PLD3^{L308P} was completely blunted, whereas the activity of PLD3^{V232M} was diminished (Figures S5I and S5K). Altogether, these results indicated that PLD3 and PLD4 form dimeric enzyme complexes and that dimer formation was required to exert catalytic activity.

A model for PLD3 interacting with an RNA substrate

To assess substrate binding in more detail, we generated a PLD3 mutant in which both catalytically relevant histidines were exchanged for asparagines (PLD3^{H201N,H416N}). As expected, recombinant PLD3^{H201N,H416N} was no longer able to process RNA (Figure 6A). To explore nucleic acid binding of this mutant, we conducted fluorescence anisotropy experiments in which we compared a 19-nt DNA and RNA oligonucleotide (Figure 6B). Both DNA and RNA exhibited high-affinity binding, yet with RNA showing slightly higher affinity (Figure 6B). Testing RNA oligonucleotides that were successively shortened by 2-nt each revealed that at least 13 nt were required for binding (Figure 6C). In fact, an 11-nt ORN showed no PLD3 binding. Conducting comparable assays with shortened DNA oligonucleotides confirmed that at least 13 nt were required for binding (Figures S6A and S6B). To pinpoint essential residues involved in nucleic acid substrate recognition, we performed calculations of the electrostatic surface potential of the PLD3 dimer at pH 5. The surface indicated two positively charged areas, one close to the active site cavity and a second area in the dimer interface (Figure 6D). Prediction of ssRNA binding to PLD3 using the Hdock server[29] confirmed the possible involvement of both these areas in nucleic acid recognition (Figure 6D). Closer inspection of the active site cleft and the transition region between both positively charged areas pointed us to two clusters of histidine residues (H337/H339 and H388/H390). In the dimer, H337/H339 from the PLD3$_A$ protomer and H388/H390 from the PLD3$_B$ protomer formed a positively charged patch on each side of the dimerization interface (Figure 6E). A structural overlay of the PLD3 cryo-EM structure with

the PLD4 Alphafold model verified that H337—and also the positively charged residue R340—were conserved and might play a role in nucleic acid binding in both proteins (Figure 6E, inset). Indeed, testing the binding affinity of the corresponding PLD3^{H201N,H416N,H337D} and PLD3^{H201N,H416N,R340D} mutants compared with PLD3^{H201N,H416N} by fluorescence anisotropy revealed diminished binding of the PLD3^{H201N,H416N,H337D} mutant to a 19-nt RNA substrate and nearly abolished binding of the PLD3^{H201N,H416N,R340D} mutant (Figure S6C). To further confirm the predicted binding positions, we collected several cryo-EM datasets of PLD3 with different phosphorothioate-containing substrates, e.g., 20 bases ssRNA and 20 bases ssDNA. Although some of the datasets showed a clear additional signal in the 2D classes (Figures 6F and 6G), the quality of the model was not sufficient to build an atomic model of the ssRNA/-DNA, respectively. However, the cryo-EM density validated the involvement of the positively charged cleft, residue H337, and presumably R340 in substrate recognition (Figure 6F). Indeed, mutation of H337/H339 revealed that this cluster was relevant for the catalytic activity of PLD3, with an approximate 10-fold reduction in enzymatic activity (Figure 6H). Single mutants of either H337 or H339 showed that H337 was especially necessary for the exonucleolytic activity of PLD3 (Figure 6I), which was also in line with its conservation in PLD4 (Figure 6E). Mutagenesis of the second patch (H388/H390) revealed a minor contribution of this site (Figures S6D and S6E), with respective single mutants behaving like the WT enzyme. Moreover, activity assays using DNA as a substrate confirmed these findings (Figures S6F and S6G).

A second site that caught our attention was tyrosine 411 (Y411)—phenylalanine in PLD4 (F423)—that is positioned above the active site (Figure 6E). Because these residues are capable of π-stacking interactions with ssRNA/-DNA, commonly seen in nucleotide binding sites and protein-DNA interactions, we also tested a PLD3 mutant for this residue (PLD3^{Y411A}). Indeed, in line with this hypothesis, PLD3^{Y411A} exerted considerably lower exonucleolytic activity toward RNA (Figure 6J) and DNA (Figure S6H). Taken together, these results indicate that PLD3 requires a minimum footprint of 13 nt for nucleic acid binding, a size that is well in agreement with the proposed nucleotide binding model and the necessity of the PLD3 dimer. In addition, the cryo-EM and biophysical properties were used to identify residues relevant to enzyme function.

DISCUSSION

Here, we showed that RNA recognition via TLR7 required the concerted activity of the endonuclease RNase T2 together with the exonucleases PLD3 and PLD4. In summary our results suggest the following model: complex RNA molecules localized to the endolysosomal compartment are first processed by endonucleases, which then expose new 5′ ends, making these fragments accessible to the 5′ exonucleases PLD3 and PLD4. The critical endonuclease in this context is RNase T2, which generates fragments that are terminated with a 2′,3′-cGMP. The resulting 3′-terminal 2′,3′-cGMP becomes the endogenous pocket 1 ligand for TLR7. The non-redundant role of RNase T2 in this process can be attributed to its unique functionality of cleaving after guanosines, which is not achieved by endonucleases of the RNase A family of enzymes. However, as an endonuclease, RNase T2 cannot process at the termini of an RNA molecule. As such, this process depends on the activity of an exonuclease to release the 3′-terminal 2′,3′-cGMP. In the endolysosomal compartment, this function is performed by the PLD exonucleases. While these enzymes primarily release 3′-NMPs from processed RNA, preprocessing of RNA by lysosomal endonucleases produces the aforementioned 2′,3′-cNMP-terminated RNA fragments, and complete processing of such a fragment releases a 2′,3′-cNMP as the final nucleotide. Consistent with this notion, RNase T2-deficient cells lacked 2′,3′-cGMP upon stimulation and their RNA-sensing defect could be overcome by directly providing 2′,3′-cGMP. PLD-deficient cells also failed to produce 2′,3′-cGMP upon stimulation but, interestingly, they could not be rescued by direct application of 2′,3′-cGMP. This raised the question of how PLD activity might be additionally involved in TLR7 activation and pointed our attention to their role in generating pocket 2 agonistic RNA fragments. Examination of RNA oligonucleotide processing at limiting enzyme concentrations revealed that PLDs stall at specific sites, preferably cytosine-rich RNAs. This implies that PLDs do not necessarily degrade the entire pool of RNA molecules to the single nucleotide level. Consistent with the notion that such fragments are the missing component for TLR7 activation, provision of such RNA molecules in *trans* together with 2′,3′-cGMP complemented the defect of PLD deficiency. R848 activity, as a hyper-physiological pocket 1 agonist, was also diminished in its stimulatory activity when PLDs were absent. It is therefore plausible that PLDs provide a constant level of pocket 2 ligands required for optimal TLR7 activation.

PLD4 is largely restricted to pDCs, whereas PLD3 is more broadly expressed, particularly in the myeloid lineage. Like pDCs, CAL-1 cells also exhibit higher PLD4 expression, but only to the extent that the higher catalytic activity of PLD3 would be balanced. Indeed, when we compared the release of 2′,3′-cGMP at CAL-1-adjusted PLD expression levels, we observed a similar release of this nucleotide by PLD3 or PLD4. Therefore, one would expect that PLD3 and PLD4 are redundantly used in these cells. However, by ablating PLD4 only in CAL-1 cells, we observed a complete loss of TLR7 RNA response in four of several cell clones tested. Interestingly, the remaining PLD3 activity in these cells still suppressed the DNA response, arguing for sufficient DNA exonuclease activity within the lysosome. Although we have not formally compared the exonuclease activity of PLD3 and PLD4 toward DNA, our data suggest that the specific activity of PLD3 toward DNA over RNA is higher than that of PLD4. Moreover, it is plausible that there are additional determinants within the lysosomal compartment that are not captured by the *in vitro* assays (e.g., post-translational modifications or cofactors) that contribute to a ''DNA preference'' of PLD3. Such a scenario could explain why loss of PLD4 shows a preferential lack of RNA response, while DNA degradation is still maintained. However, we also identified two PLD4-deficient clones that exhibited partial or full RNA response, suggesting that there is a substantial increase in PLD3 activity that functionally compensates for the absence of PLD4. Consistent with this, by overexpressing PLD3 in *PLD3*$^{-/-}$ × *PLD4*$^{-/-}$ cells, we were able to partially restore the RNA response in these cells. In general, it appears that the CAL-1 system operates at the edge where both PLD enzyme

activities play a role. It is unlikely that such a scenario is relevant in primary pDC, where PLD4 expression significantly exceeds PLD3 expression, or in myeloid cells, where the reverse scenario applies. Indeed, we observed almost completely attenuated TLR7 responses in the absence of PLD3 in primary human-monocyte-derived macrophages and in J774 mouse macrophages. This indicates that, in myeloid cells, PLD3 is the predominant exonuclease that also operates to generate TLR7 agonistic ligands.

Notably, previous work on the immunological functions of PLDs has established that PLDs can negatively regulate immune responses by limiting nucleic acid ligand availability.[17,18,30] Thus, mice deficient in both PLD3 and PLD4 display a prominent autoinflammatory response that can be rescued by ablating the function of nucleic-acid-sensing TLRs (UNC93B1 deficiency). In this model, lack of both PLD3 and PLD4 was required to unleash the inflammatory response, suggesting redundant functions of these exonucleases in nucleic acid degradation. Moreover, single deficiency of TLR9 was unable to fully rescue the phenotype,[18] suggesting an involvement of the RNA-sensing TLR systems. In support of this notion, mice with a gene dosage increase in TLR7 showed an increased inflammatory response when PLD4 was ablated. *In vitro* experiments with RNA oligonucleotides in part supported the negative regulatory role of PLDs for TLR7 and TLR13 stimulation—but with certain inconsistencies. For example, while TLR13 responses were generally increased, certain TLR7-agonistic RNA oligonucleotides showed increased or unchanged responses in $PLD3^{-/-} \times PLD4^{-/-}$ cells, and some responses were even decreased. Nevertheless, in line with the *in vivo* experiments, it was concluded that PLDs can either negatively regulate TLR7 responses similarly to TLR9 or positively regulate TLR7 responses, depending on the substrate. Our data indicate a requirement for PLD exonuclease activity for TLR7 activation, which seems to contrast the aforementioned work. However, it needs to be considered that our work focuses on the cell-intrinsic role of PLD exonucleases in TLR7 activation and not on the *in vivo* role. This is important because, *in vivo*, additional mechanisms may be involved that are secondary to the defect under study. Consistent with this notion, RNase T2[31] or DNase 2[32] deficiency induces prominent inflammatory responses *in vivo*, whereas these nucleases play a productive role in the production of TLR7/8[12,13] or TLR9[33] ligands at the cell-autonomous level. Another important consideration is that previous studies have focused on murine macrophages, which have a different expression pattern of PLDs and nucleic-acid-sensing TLRs, and that most of the mechanistic studies were conducted with phosphorothioate oligonucleotides that display a clear cell type and cell-type specificity.

Our structural and biochemical studies led to the unexpected finding that both PLD3 and PLD4 form homodimers. Although homodimer formation is well described for several PLD family enzymes, these are enzymes that contain only one HxK motif and require dimerization to form a functional catalytic center.[34] Because PLD3 and PLD4 contain two HxKxxxxD/E motif-containing lobes by internal domain duplication, dimerization should not be necessary to achieve enzymatic activity. However, it appears that dimer formation is needed to create a binding site involving both PLD protomers. These results are also consistent with the notion that nucleic acid molecules below 13 nt do not bind PLD3, a molecular footprint consistent with the requirement of two protomers for binding. While this paper was under review, another structure of PLD3 was reported,[35] supporting the finding that PLD3 forms homodimers. In contrast to our findings, binding of short oligonucleotides (5 nt in length) were reported, yet with significantly lower binding affinities compared with our long substrates. Subsequently, an alternative oligomer binding site was proposed that would not rely on the dimerization of PLD3 to bind to ssDNA, contrasting with our binding model. However, considering that PLD3 is targeted to the acidic lysosomal compartment, we examined the electrostatic surface potential of PLD3 at pH 5. Our analysis revealed two distinct positively charged regions not previously identified, suggesting a potential binding site for long nucleic acids involving both protomers of the dimer, which we could confirm by biochemical studies. Our results would be consistent with a model in which the activity of PLD exonucleases is divided into a distributive and a processive phase, as has been reported for other exonucleases.[36] In the initial distributive phase, the PLDs would show a strong preference for longer RNA sequences, >11 nucleotides in length. During this phase, they would bind to an RNA molecule, cleave a few nucleotides, and then release the RNA before binding to another substrate. This intermittent mode of action would be dictated by the enzyme's higher affinity for longer RNA molecules. As the enzyme progresses to the second phase, it undergoes a change in its mechanism and becomes highly processive. In this phase, once the exonuclease binds to its preferred longer RNA substrates, it stays attached and sequentially cleaves nucleotides, completely processing the RNA in a single binding event. Adverse substrates (e.g., secondary structure and sequence composition) would prevent this switch in activity and remain as shorter RNA fragments. These, in turn, could serve as pocket 2 ligands for TLR7.

In conclusion, our results elucidate the intricate role of nucleases in RNA recognition by TLR7. Interestingly, the dual role of PLD exonucleases, acting both pro-inflammatory (TLR7) and anti-inflammatory (TLR9), suggests a finely tuned balance to orchestrate appropriate immune responses. The simultaneous promotion and inhibition of inflammation by these exonucleases may serve as an essential protective mechanism, shielding the host from potential microbial modulators that would perturb this system. This nuanced modulation may also have important implications for therapeutic strategies aimed at harnessing or recalibrating these immune pathways.

Limitations of the study

Our work indicates that PLD exonucleases are essential for the generation of ligands for the first and second binding pockets of TLR7. Together with RNase T2, PLD enzymes release 2′,3′-cGMP, the proposed ligand for the first binding pocket. Conversely, PLD exonucleases tend to stall at cytidines, leaving fragments suitable for the second binding pocket of TLR7. However, the exact identity of these fragments remains to be determined, indicating the need for further work in this direction. In addition, the possible involvement of other lysosomal endonucleases, such as the RNase A family, in the generation of the ligand for the second binding pocket cannot be ruled out. It is conceivable that RNase A family enzymes may also degrade ssRNAs within the lysosome that are initially too large to bind

TLR7, followed by subsequent trimming by PLD3 and PLD4, rendering them compatible for TLR7 binding.

STAR★METHODS

Detailed methods are provided in the online version of this paper and include the following:

- KEY RESOURCES TABLE
- RESOURCE AVAILABILITY
  - Lead contact
  - Materials availability
  - Data and code availability
- EXPERIMENTAL MODEL AND STUDY PARTICIPANT DETAILS
  - Cell culture
  - Cell stimulation
  - Isolation of PBMCs, primary plasmacytoid dendritic cells and primary human monocytes
  - CRISPR/ Cas9 mediated knockout generation
  - CRISPR/ Cas9 mediated knockout generation in primary human monocytes
  - Lentiviral transduction
- METHOD DETAILS
  - Immunoblotting
  - ELISA
  - Gene expression analysis
  - PLD3 and PLD4 protein purification
  - Coomassie staining of PLD3 and PLD4
  - Cryo-EM sample preparation and data acquisition of PLD3 and PLD4
  - Model building and refinement
  - Mass photometry
  - Nuclease assays
  - Urea gels
  - Affinity measurement by fluorescence anisotropy
  - Fluorescent RNA degradation assay
  - PLD3 and PLD4 quantification and whole proteome analysis
  - Preparation for LC-MS analysis of PLD3 and PLD4 degradation products
  - LC-MS/QQQ analysis of nucleoside-monophosphates
  - LC-HRMS analysis of oligonucleotides
- QUANTIFICATION AND STATISTICAL ANALYSIS

SUPPLEMENTAL INFORMATION

Supplemental information can be found online at https://doi.org/10.1016/j.immuni.2024.04.010.

ACKNOWLEDGMENTS

We kindly thank S. Suppmann and the Protein Production Core Facility (MPI, Munich) for expressing recombinant RNase 1, RNase 2, and RNase 6 and the BioSysM flow cytometry facility for great support. We thank Claudia Ludwig for technical support in isolating primary cells, Bachuki Shashikadze for his help in data analysis, and Zhiqi Sun for helpful discussions (all Gene Center, LMU). This work was supported by grants from the ERC (ERC-2020-ADG–101018672 ENGINES) to V.H., the Deutsche Forschungsgemeinschaft (DFG, German Research Foundation) CRC 237/A27 (Project-ID 369799452) to V.H. and T.C. and CRC 237/A05 (Project-ID 369799452) to K.-P.H., and the BMBF in the framework of the Cluster4future program (CNATM—Cluster for Nucleic Acid Therapeutics Munich) to T.C., K.-P.H., and V.H.

AUTHOR CONTRIBUTIONS

Conceptualization, M.B., K.L., and V.H.; investigation, M.B., K.L., M.H., L.H., S.B., J.S., F.P., I.P., W.G., M.W., C.J., and T.F.; writing – original draft, M.B., K.L., and V.H. with input from all authors; writing – review and editing, M.B. and V.H.; resources, T.C., K.-P.H., and V.H.; funding acquisition, V.H.; supervision, V.H.

DECLARATION OF INTERESTS

The authors declare no competing interests.

Received: October 16, 2023
Revised: March 6, 2024
Accepted: April 12, 2024
Published: May 1, 2024

REFERENCES

1. Diebold, S.S., Kaisho, T., Hemmi, H., Akira, S., and Reis e Sousa, C. (2004). Innate antiviral responses by means of TLR7-mediated recognition of single-stranded RNA. Science *303*, 1529–1531. https://doi.org/10.1126/science.1093616.
2. Heil, F., Hemmi, H., Hochrein, H., Ampenberger, F., Kirschning, C., Akira, S., Lipford, G., Wagner, H., and Bauer, S. (2004). Species-specific recognition of single-stranded RNA via toll-like receptor 7 and 8. Science *303*, 1526–1529. https://doi.org/10.1126/science.1093620.
3. Vinuesa, C.G., Grenov, A., and Kassiotis, G. (2023). Innate virus-sensing pathways in B cell systemic autoimmunity. Science *380*, 478–484. https://doi.org/10.1126/science.adg6427.
4. Fitzgerald, K.A., and Kagan, J.C. (2020). Toll-like Receptors and the Control of Immunity. Cell *180*, 1044–1066. https://doi.org/10.1016/j.cell.2020.02.041.
5. Lind, N.A., Rael, V.E., Pestal, K., Liu, B., and Barton, G.M. (2022). Regulation of the nucleic acid-sensing Toll-like receptors. Nat. Rev. Immunol. *22*, 224–235. https://doi.org/10.1038/s41577-021-00577-0.
6. Majer, O., Liu, B., Woo, B.J., Kreuk, L.S.M., Van Dis, E., and Barton, G.M. (2019). Release from UNC93B1 reinforces the compartmentalized activation of select TLRs. Nature *575*, 371–374. https://doi.org/10.1038/s41586-019-1611-7.
7. Majer, O., Liu, B., Kreuk, L.S.M., Krogan, N., and Barton, G.M. (2019). UNC93B1 recruits syntenin-1 to dampen TLR7 signalling and prevent autoimmunity. Nature *575*, 366–370. https://doi.org/10.1038/s41586-019-1612-6.
8. Swiecki, M., and Colonna, M. (2015). The multifaceted biology of plasmacytoid dendritic cells. Nat. Rev. Immunol. *15*, 471–485. https://doi.org/10.1038/nri3865.
9. Zhang, Z., Ohto, U., Shibata, T., Krayukhina, E., Taoka, M., Yamauchi, Y., Tanji, H., Isobe, T., Uchiyama, S., Miyake, K., and Shimizu, T. (2016). Structural Analysis Reveals that Toll-like Receptor 7 Is a Dual Receptor for Guanosine and Single-Stranded RNA. Immunity *45*, 737–748. https://doi.org/10.1016/j.immuni.2016.09.011.
10. Zhang, Z., Ohto, U., Shibata, T., Taoka, M., Yamauchi, Y., Sato, R., Shukla, N.M., David, S.A., Isobe, T., Miyake, K., and Shimizu, T. (2018). Structural Analyses of Toll-like Receptor 7 Reveal Detailed RNA Sequence Specificity and Recognition Mechanism of Agonistic Ligands. Cell Rep. *25*, 3371–3381.e5. https://doi.org/10.1016/j.celrep.2018.11.081.
11. Tanji, H., Ohto, U., Shibata, T., Taoka, M., Yamauchi, Y., Isobe, T., Miyake, K., and Shimizu, T. (2015). Toll-like receptor 8 senses degradation products of single-stranded RNA. Nat. Struct. Mol. Biol. *22*, 109–115. https://doi.org/10.1038/nsmb.2943.
12. Greulich, W., Wagner, M., Gaidt, M.M., Stafford, C., Cheng, Y., Linder, A., Carell, T., and Hornung, V. (2019). TLR8 Is a Sensor of RNase T2 Degradation Products. Cell *179*, 1264–1275.e13. https://doi.org/10.1016/j.cell.2019.11.001.
13. Ostendorf, T., Zillinger, T., Andryka, K., Schlee-Guimaraes, T.M., Schmitz, S., Marx, S., Bayrak, K., Linke, R., Salgert, S., Wegner, J., et al. (2020). Immune Sensing of Synthetic, Bacterial, and Protozoan RNA by Toll-like Receptor 8 Requires Coordinated Processing by RNase T2 and RNase 2. Immunity *52*, 591–605.e6. https://doi.org/10.1016/j.immuni.2020.03.009.

14. Liu, K., Sato, R., Shibata, T., Hiranuma, R., Reuter, T., Fukui, R., Zhang, Y., Ichinohe, T., Ozawa, M., Yoshida, N., et al. (2021). Skewed endosomal RNA responses from TLR7 to TLR3 in RNase T2-deficient macrophages. Int. Immunol. *33*, 479–490. https://doi.org/10.1093/intimm/dxab033.

15. Maeda, T., Murata, K., Fukushima, T., Sugahara, K., Tsuruda, K., Anami, M., Onimaru, Y., Tsukasaki, K., Tomonaga, M., Moriuchi, R., et al. (2005). A novel plasmacytoid dendritic cell line, CAL-1, established from a patient with blastic natural killer cell lymphoma. Int. J. Hematol. *81*, 148–154. https://doi.org/10.1532/ijh97.04116.

16. Hornung, V., Guenthner-Biller, M., Bourquin, C., Ablasser, A., Schlee, M., Uematsu, S., Noronha, A., Manoharan, M., Akira, S., de Fougerolles, A., et al. (2005). Sequence-specific potent induction of IFN-alpha by short interfering RNA in plasmacytoid dendritic cells through TLR7. Nat. Med. *11*, 263–270. https://doi.org/10.1038/nm1191.

17. Gavin, A.L., Huang, D., Huber, C., Mårtensson, A., Tardif, V., Skog, P.D., Blane, T.R., Thinnes, T.C., Osborn, K., Chong, H.S., et al. (2018). PLD3 and PLD4 are single-stranded acid exonucleases that regulate endosomal nucleic-acid sensing. Nat. Immunol. *19*, 942–953. https://doi.org/10.1038/s41590-018-0179-y.

18. Gavin, A.L., Huang, D., Blane, T.R., Thinnes, T.C., Murakami, Y., Fukui, R., Miyake, K., and Nemazee, D. (2021). Cleavage of DNA and RNA by PLD3 and PLD4 limits autoinflammatory triggering by multiple sensors. Nat. Commun. *12*, 5874. https://doi.org/10.1038/s41467-021-26150-w.

19. Hao, Y., Hao, S., Andersen-Nissen, E., Mauck, W.M., 3rd, Zheng, S., Butler, A., Lee, M.J., Wilk, A.J., Darby, C., Zager, M., et al. (2021). Integrated analysis of multimodal single-cell data. Cell *184*, 3573–3587.e29. https://doi.org/10.1016/j.cell.2021.04.048.

20. Speir, M.L., Bhaduri, A., Markov, N.S., Moreno, P., Nowakowski, T.J., Papatheodorou, I., Pollen, A.A., Raney, B.J., Seninge, L., Kent, W.J., and Haeussler, M. (2021). UCSC Cell Browser: visualize your single-cell data. Bioinformatics *37*, 4578–4580. https://doi.org/10.1093/bioinformatics/btab503.

21. Zhang, S., Hu, Z., Tanji, H., Jiang, S., Das, N., Li, J., Sakaniwa, K., Jin, J., Bian, Y., Ohto, U., et al. (2018). Small-molecule inhibition of TLR8 through stabilization of its resting state. Nat. Chem. Biol. *14*, 58–64. https://doi.org/10.1038/nchembio.2518.

22. Cappel, C., Gonzalez, A.C., and Damme, M. (2021). Quantification and characterization of the 5′ exonuclease activity of the lysosomal nuclease PLD3 by a novel cell-based assay. J. Biol. Chem. *296*, 100152. https://doi.org/10.1074/jbc.RA120.015867.

23. Bowling, F.Z., Salazar, C.M., Bell, J.A., Huq, T.S., Frohman, M.A., and Airola, M.V. (2020). Crystal structure of human PLD1 provides insight into activation by PI(4,5)P(2) and RhoA. Nat. Chem. Biol. *16*, 400–407. https://doi.org/10.1038/s41589-020-0499-8.

24. Gottlin, E.B., Rudolph, A.E., Zhao, Y., Matthews, H.R., and Dixon, J.E. (1998). Catalytic mechanism of the phospholipase D superfamily proceeds via a covalent phosphohistidine intermediate. Proc. Natl. Acad. Sci. USA *95*, 9202–9207. https://doi.org/10.1073/pnas.95.16.9202.

25. Stuckey, J.A., and Dixon, J.E. (1999). Crystal structure of a phospholipase D family member. Nat. Struct. Biol. *6*, 278–284. https://doi.org/10.1038/6716.

26. Jumper, J., Evans, R., Pritzel, A., Green, T., Figurnov, M., Ronneberger, O., Tunyasuvunakool, K., Bates, R., Žídek, A., Potapenko, A., et al. (2021). Highly accurate protein structure prediction with AlphaFold. Nature *596*, 583–589. https://doi.org/10.1038/s41586-021-03819-2.

27. Cruchaga, C., Karch, C.M., Jin, S.C., Benitez, B.A., Cai, Y., Guerreiro, R., Harari, O., Norton, J., Budde, J., Bertelsen, S., et al. (2014). Rare coding variants in the phospholipase D3 gene confer risk for Alzheimer's disease. Nature *505*, 550–554. https://doi.org/10.1038/nature12825.

28. Nibbeling, E.A.R., Duarri, A., Verschuuren-Bemelmans, C.C., Fokkens, M.R., Karjalainen, J.M., Smeets, C.J.L.M., de Boer-Bergsma, J.J., van der Vries, G., Dooijes, D., Bampi, G.B., et al. (2017). Exome sequencing and network analysis identifies shared mechanisms underlying spinocerebellar ataxia. Brain *140*, 2860–2878. https://doi.org/10.1093/brain/awx251.

29. Yan, Y., Tao, H., He, J., and Huang, S.Y. (2020). The HDOCK server for integrated protein-protein docking. Nat. Protoc. *15*, 1829–1852. https://doi.org/10.1038/s41596-020-0312-x.

30. Van Acker, Z.P., Perdok, A., Hellemans, R., North, K., Vorsters, I., Cappel, C., Dehairs, J., Swinnen, J.V., Sannerud, R., Bretou, M., et al. (2023). Phospholipase D3 degrades mitochondrial DNA to regulate nucleotide signaling and APP metabolism. Nat. Commun. *14*, 2847. https://doi.org/10.1038/s41467-023-38501-w.

31. Kettwig, M., Ternka, K., Wendland, K., Krüger, D.M., Zampar, S., Schob, C., Franz, J., Aich, A., Winkler, A., Sakib, M.S., et al. (2021). Interferon-driven brain phenotype in a mouse model of RNaseT2 deficient leukoencephalopathy. Nat. Commun. *12*, 6530. https://doi.org/10.1038/s41467-021-26880-x.

32. Kawane, K., Ohtani, M., Miwa, K., Kizawa, T., Kanbara, Y., Yoshioka, Y., Yoshikawa, H., and Nagata, S. (2006). Chronic polyarthritis caused by mammalian DNA that escapes from degradation in macrophages. Nature *443*, 998–1002. https://doi.org/10.1038/nature05245.

33. Chan, M.P., Onji, M., Fukui, R., Kawane, K., Shibata, T., Saitoh, S., Ohto, U., Shimizu, T., Barber, G.N., and Miyake, K. (2015). DNase II-dependent DNA digestion is required for DNA sensing by TLR9. Nat. Commun. *6*, 5853. https://doi.org/10.1038/ncomms6853.

34. Yang, W. (2011). Nucleases: diversity of structure, function and mechanism. Q. Rev. Biophys. *44*, 1–93. https://doi.org/10.1017/S0033583510000181.

35. Roske, Y., Cappel, C., Cremer, N., Hoffmann, P., Koudelka, T., Tholey, A., Heinemann, U., Daumke, O., and Damme, M. (2024). Structural analysis of PLD3 reveals insights into the mechanism of lysosomal 5′ exonuclease-mediated nucleic acid degradation. Nucleic Acids Res. *52*, 370–384. https://doi.org/10.1093/nar/gkad1114.

36. Ye, X., Axhemi, A., and Jankowsky, E. (2021). Alternative RNA degradation pathways by the exonuclease Pop2p from Saccharomyces cerevisiae. RNA *27*, 465–476. https://doi.org/10.1261/rna.078006.120.

37. Rapino, F., Robles, E.F., Richter-Larrea, J.A., Kallin, E.M., Martinez-Climent, J.A., and Graf, T. (2013). C/EBPalpha induces highly efficient macrophage transdifferentiation of B lymphoma and leukemia cell lines and impairs their tumorigenicity. Cell Rep. *3*, 1153–1163. https://doi.org/10.1016/j.celrep.2013.03.003.

38. Jack, I., Seshadri, R., Garson, M., Michael, P., Callen, D., Zola, H., and Morley, A. (1986). RCH-ACV: a lymphoblastic leukemia cell line with chromosome translocation 1;19 and trisomy 8. Cancer Genet. Cytogenet. *19*, 261–269. https://doi.org/10.1016/0165-4608(86)90055-5.

39. Schmidt, T., Schmid-Burgk, J.L., and Hornung, V. (2015). Synthesis of an arrayed sgRNA library targeting the human genome. Sci. Rep. *5*, 14987. https://doi.org/10.1038/srep14987.

40. Schmid-Burgk, J.L., Schmidt, T., Gaidt, M.M., Pelka, K., Latz, E., Ebert, T.S., and Hornung, V. (2014). OutKnocker: a web tool for rapid and simple genotyping of designer nuclease edited cell lines. Genome Res. *24*, 1719–1723. https://doi.org/10.1101/gr.176701.114.

41. Li, Z., Michael, I.P., Zhou, D., Nagy, A., and Rini, J.M. (2013). Simple piggyBac transposon-based mammalian cell expression system for inducible protein production. Proc. Natl. Acad. Sci. USA *110*, 5004–5009. https://doi.org/10.1073/pnas.1218620110.

42. Punjani, A., Rubinstein, J.L., Fleet, D.J., and Brubaker, M.A. (2017). cryoSPARC: algorithms for rapid unsupervised cryo-EM structure determination. Nat. Methods *14*, 290–296. https://doi.org/10.1038/nmeth.4169.

43. Bepler, T., Morin, A., Rapp, M., Brasch, J., Shapiro, L., Noble, A.J., and Berger, B. (2019). Positive-unlabeled convolutional neural networks for particle picking in cryo-electron micrographs. Nat. Methods *16*, 1153–1160. https://doi.org/10.1038/s41592-019-0575-8.

44. Emsley, P., Lohkamp, B., Scott, W.G., and Cowtan, K. (2010). Features and development of Coot. Acta Crystallogr. D Biol. Crystallogr. *66*, 486–501. https://doi.org/10.1107/S0907444910007493.

45. Croll, T.I. (2018). ISOLDE: a physically realistic environment for model building into low-resolution electron-density maps. Acta Crystallogr. D Struct. Biol. *74*, 519–530. https://doi.org/10.1107/S2059798318002425.

46. Liebschner, D., Afonine, P.V., Baker, M.L., Bunkóczi, G., Chen, V.B., Croll, T.I., Hintze, B., Hung, L.W., Jain, S., McCoy, A.J., et al. (2019). Macromolecular structure determination using X-rays, neutrons and electrons: recent developments in Phenix. Acta Crystallogr. D Struct. Biol. *75*, 861–877. https://doi.org/10.1107/S2059798319011471.

47. Afonine, P.V., Grosse-Kunstleve, R.W., Echols, N., Headd, J.J., Moriarty, N.W., Mustyakimov, M., Terwilliger, T.C., Urzhumtsev, A., Zwart, P.H., and Adams, P.D. (2012). Towards automated crystallographic structure refinement with phenix.refine. Acta Crystallogr. D Biol. Crystallogr. *68*, 352–367. https://doi.org/10.1107/S0907444912001308.

48. Pettersen, E.F., Goddard, T.D., Huang, C.C., Meng, E.C., Couch, G.S., Croll, T.I., Morris, J.H., and Ferrin, T.E. (2021). UCSF ChimeraX: Structure visualization for researchers, educators, and developers. Protein Sci. *30*, 70–82. https://doi.org/10.1002/pro.3943.

49. Jung, C., Bandilla, P., von Reutern, M., Schnepf, M., Rieder, S., Unnerstall, U., and Gaul, U. (2018). True equilibrium measurement of transcription factor-DNA binding affinities using automated polarization microscopy. Nat. Commun. *9*, 1605. https://doi.org/10.1038/s41467-018-03977-4.

50. Shashikadze, B., Valla, L., Lombardo, S.D., Prehn, C., Haid, M., Riols, F., Stöckl, J.B., Elkhateib, R., Renner, S., Rathkolb, B., et al. (2023). Maternal hyperglycemia induces alterations in hepatic amino acid, glucose and lipid metabolism of neonatal offspring: multi-omics insights from a diabetic pig model. Mol. Metab. *75*, 101768. https://doi.org/10.1016/j.molmet.2023.101768.

51. Demichev, V., Messner, C.B., Vernardis, S.I., Lilley, K.S., and Ralser, M. (2020). DIA-NN: neural networks and interference correction enable deep proteome coverage in high throughput. Nat. Methods *17*, 41–44. https://doi.org/10.1038/s41592-019-0638-x.

52. Pino, L.K., Searle, B.C., Bollinger, J.G., Nunn, B., MacLean, B., and MacCoss, M.J. (2020). The Skyline ecosystem: Informatics for quantitative mass spectrometry proteomics. Mass Spectrom. Rev. *39*, 229–244. https://doi.org/10.1002/mas.21540.

STAR★METHODS

KEY RESOURCES TABLE

REAGENT or RESOURCE	SOURCE	IDENTIFIER
Antibodies		
Anti-TLR7	Cell Signaling Technology	Cat#5632 RRID:AB_10692895
Anti-β actin	Santa Cruz Biotechnologies	Cat#47778 RRID:AB_2714189
Direct-Blot HRP anti FLAG tag	BioLegend	Cat#637311 RRID:AB_2566706
Anti-rabbit IgG HRP linked	Cell Signaling Technology	Cat#7074 RRID:AB_2099233
Chemicals, peptides, and recombinant proteins		
Acetonitrile	Carl Roth	Cat# HN40.1
Advanced RPMI 1640 medium	Gibco	Cat# 12633020
Ammonium persulfate	Sigma-Aldrich	Cat# A3678
BioColl	Bio&Sell	Cat# BS.L 6115
Blasticidin	Thermo Scientific	Cat# A1113903
CD14 MircroBeads Human	Miltenyi	Cat# 130-050-201
Coomassie Brilliant Blue R-250 Dye	Thermo Scientific	Cat# 20278
CU-CPT9a	Invivogen	Cat# inh-cc9a
Doxycycline	Sigma-Aldrich	Cat# D9891
Fetal calf serum	Gibco	Cat# 10270106
GlutaMAX	Gibco	Cat# 35050038
HEPES	Sigma-Aldrich	Cat# H0887-100ML
LPS-EB Ultrapure	InvivoGen	Cat#tlrl-3pelps
Lys-C	Wako	Cat# 4548995075888
MEM NEAA	Gibco	Cat# 11140035
Modified porcine trypsin	Promega	Cat# VA9000
NI-NTA agarose beads	Quiagen	Cat# R90115
Nitrocellulose membrane (0.45 μm)	GE Healthcare	Cat#10600002
Opti-MEM™	Gibco	Cat# 31985047
Penicillin/Streptomycin	Gibco	Cat# 15-140-122
PepMap 100 C18 trap column	Thermo Fisher Scientific	Cat#164750
PepMap RSLC C18	Thermo Fisher Scientific	Cat#164540
PLD3 peptides: ALLNVVDNAX (A310 to R319) LFVVPADEAQAX (L397 to R408) SQLEAIFLX (S458 to R466)	JPT Peptide Technologies	N/A
PLD4 peptides: LQQLLGX (L164 to R170) FWVVDGX (F217 to R223)	JPT Peptide Technologies	N/A
Poly-L-arginine	Sigma-Aldrich	Cat#P7762
Puromycin	Carl Roth	Cat# 0240.4
Recombinant Human IL-3	MPI of Biochemistry, Munich	N/A
Recombinant Human IFN-γ	PeproTech	Cat#300-02
Recombinant Human CSF1 (M-CSF)	MPI of Biochemistry, Munich	N/A
Recombinant PreScission Protease	MPI of Biochemistry, Munich	N/A
Recombinant Human PLD3 (and all PLD3 mutants)	This Paper	N/A
Recombinant Human PLD4	This Paper	N/A
Recombinant Human RNase 1	MPI of Biochemistry, Munich	N/A
Recombinant Human RNase 2	MPI of Biochemistry, Munich	N/A
Recombinant Human RNase 6	MPI of Biochemistry, Munich	N/A

(*Continued on next page*)

Continued

REAGENT or RESOURCE	SOURCE	IDENTIFIER
RBC lysis Buffer	BioLegend	Cat# 420301
RPMI 1640 medium	Gibco	Cat# 11875093
R848	InvivoGen	Cat# tlrl-r848
SequaGel Concentrate	National diagnostics	Cat#EC830-1L
SequaGel Buffer	National diagnostics	Cat# EC835-200ml
SequaGel Diluent	National diagnostics	Cat# EC840-1L
Sodium pyruvate	Gibco	Cat# 11360039
Superdex-200 increase 5/50 GL	Sigma-Aldrich	Cat# 28-9909-45
SYBR Gold Nucleic Acid Gel Stain	Thermo Fisher Scientifc	Cat# S33102
TEMED	Carl Roth	Cat# 2367.3
TL8-506	InvivoGen	Cat# tlrl-tl8506
TRIS glycine SDS-PAGE	Thermo Scientific	Cat# XP00125BOX
cOmplete	Roche	Cat# CO-RO
β-Estradiol	Sigma-Aldrich	Cat#E8875
2',3'-cGMP	BIOLOG	Cat# G 025-250
3'-GMP	BIOLOG	Cat# G 021-50
5'-GMP	Sigma Aldrich	Cat # G8377
2x RNA loading dye	Thermo Fisher Scientific	Cat# R0641
Critical commercial assays		
Human IFN-βELISA Set	R&D System	Cat# DY814-05
Human IFN-α2 ELISA Set	R&D System	Cat# DY9345-05
Human IL-6 ELISA Set	BD Biosciences	Cat# 555220
Human TNF ELISA Set	BD Biosciences	Cat# 555212
Mouse IL-6 ELISA Set	BD Biosciences	Cat# 555240
BCA protein assay Kit	Thermo Fisher Scientific	Cat# 23227
CD34 MicroBead Kit UltraPure, human	Miltenyi	Cat# 130-100-453
PAN Monocyte Isolation Kit	Miltenyi	Cat# 130-096-537
SG Cell Line 96-well NucleofectorTM Kit	Lonza	Cat# V4SC-3096
P3 Primary Cell 4D-Nucleofector X Kit S	Lonza	Cat# V4XP-3032
MiSeq Reagent Kit v2, 300 Cycles	Illumina	Cat# MS-102-2002
Deposited data		
Mass spectrometry proteomics	ProteomeXchange Consortium	PXD045912
Experimental models: Cell lines		
CAL-1	Maeda et al.[15]	N/A
BLaER1 human b-cell to monocyte trans-differentiation cell line	Rapino et al.[37]	N/A
RCH-ACV	Jack et al.[38]	N/A
Oligonucleotides		
RNA40S(rG*rC*rC*rC*rG*rU*rC*rU*rG*rU*rU*rG*rU*rG*rU*rG*rA*rC*rU*rC)	Miltenyi	130-104-429
RNA40 (rGrCrCrCrGrUrCrUrGrUrUrGrUrGrUrGrArCrUrC)	IDT	N/A
RNA9.2s (rArGrCrUrUrArArCrCrUrGrUrCrCrUrUrCrArA)	IDT	N/A
CpG^S (T*C*G*T*C*G*T*T*T*T*G*T*C*G*T*T*T*T*G*T*C*G*T*T)	IDT	N/A
CpG^O (TCGTCGTTTTGTCGTTTTGTCGTT)	IDT	N/A
$rCrCrUrUrCrA(AC)_7$	IDT	N/A
$rArArUrUrCrA(AC)_7$	IDT	N/A
$rUrUrUrUrU(AC)_7$	IDT	N/A
rGrUrArGrArGrArGrArGrArGrArGrArGrArG	IDT	N/A
rArGrUrArGrArGrArGrArGrArGrArGrArGrA	IDT	N/A
rGrArGrUrArGrArGrArGrArGrArGrArGrArG	IDT	N/A
rArGrArGrUrArGrArGrArGrArGrArGrArGrA	IDT	N/A

(*Continued on next page*)

Continued

REAGENT or RESOURCE	SOURCE	IDENTIFIER
$(rU*rC*)_{10}$	IDT	N/A
$(A*C*)_{10}$	IDT	N/A
5'-FAM-RNA40-3'-BMNQ530 (rGrCrCrCrGrUrCrUrGrUrUrGrUrGrUrGrArCrUrC)	Biomers	N/A
RNA9.2s-3'FAM (rArGrCrUrUrArArCrCrUrGrUrCrCrUrUrCrArA-FAM)	Metabion	N/A
rArGrCrUrUrArArCrCrUrGrUrCrCrUrUrC-FAM	Metabion	N/A
rArGrCrUrUrArArCrCrUrGrUrCrCrU-FAM	Metabion	N/A
rArGrCrUrUrArArCrCrUrGrUrC-FAM	Metabion	N/A
rArGrCrUrUrArArCrCrUrG-FAM	Metabion	N/A
rArGrCrUrUrArArCrC-FAM	Metabion	N/A
rArGrCrUrUrArA-FAM	Metabion	N/A
rArGrCrUrU-FAM	Metabion	N/A
DNA9.2s-3'FAM (AGCTTAACCTGTCCTTCAA-FAM)	Metabion	N/A
AGCTTAACCTGTCCTTC-FAM	Metabion	N/A
AGCTTAACCTGTCCT-FAM	Metabion	N/A
AGCTTAACCTGTC-FAM	Metabion	N/A
AGCTTAACCTG-FAM	Metabion	N/A
AGCTTAACC-FAM	Metabion	N/A
Recombinant DNA		
PB_6xHis_hsPLD3 (and all mutants)	This study	N/A
PB_6xHis_hsPLD4	This study	N/A
pFUGW_hsPLD3_Blast	This study	N/A
pCAS9-mCherry-gRNA	Schmidt et al.[39]	N/A
Software and algorithms		
GraphPad Prism10	GraphPad	N/A
Outknocker	Schmid-Burgk et al.[40]	N/A
ChimeraX	UCSF ChimeraX	N/A
AcquireMP	Refeyn	N/A
MassHunter Software	Agilent	N/A
Other		
384W SensoPlate™, Sterile, Flat Bottom, Black/Glass, w/Lid	Greiner Bio-One	Cat# 781892

RESOURCE AVAILABILITY

Lead contact

Further information and requests for resources and reagents should be directed to and will be fulfilled by the lead contact, Veit Hornung (hornung@genzentrum.lmu.de).

Materials availability

All newly generated materials associated with the paper are available upon request from the lead contact.

Data and code availability

- Raw MS data is deposited in PRIDE database under accession number PXD045912.
- The coordinates of the PLD3 apoenzyme structure have been deposited in the Protein Data Bank (PDB) under the accession number 8S86 and the cryo-EM reconstruction is available in the Electron Microscopy Data Bank (EMDB) under the EMBD accession number EMD-19798.
- This paper does not report original code.
- Any additional information required to reanalyze the data reported in this work paper is available from the lead contact upon request.

EXPERIMENTAL MODEL AND STUDY PARTICIPANT DETAILS

Cell culture

CAL-1 cells, which were derived from a male donor (hemizygous for TLR7), were cultured in RPMI 1640 medium supplemented with 10% heat-inactivated fetal calf serum, 100 U/ ml penicillin/streptomycin (PS), 1 mM sodium pyruvate, 2 x GlutaMAX, 10 mM HEPES and 1 x MEM NEAA.

BLaER1 monocytes, which were derived from a female donor, RCH-ACV cells and primary plasmacytoid dendritic cells were cultured in RPMI 1640 medium, supplemented with 10% heat-inactivated fetal calf serum (FCS), 100 U/ ml penicillin/streptomycin (PS) and 1 mM sodium pyruvate. Primary monocytes were cultured in RPMI 1640 medium, supplemented with 10% FCS, 2 mM GlutaMAX and 100 U/ ml penicillin/streptomycin (PS). J774 mouse macrophages were cultured in DMEM medium supplemented with 10% heat-inactivated fetal calf serum (FCS), 100 U/ ml penicillin/streptomycin (PS) and 1 mM sodium pyruvate. All cells were cultured in a humidified incubator at 37 °C with 5% CO_2. For trans-differentiation of BLaER1 monocytes into macrophages, the cytokines M-CSF (10 ng/ml), IL-3 (10 ng/ml) and 100 nM β-estradiol were added to the culture media. Cells were differentiated in a 96-well plate (80,000 cells/well) for 5 days and afterwards used for stimulation experiments. For differentiation of primary monocytes into macrophages, the cytokine M-CSF (100 ng/ml) was added to the culture medium. Cells were differentiated in non-treated 6 well plates ($1x10^6$ cells/well) for 8 days and fresh M-CSF was added every 2 days.

Cell stimulation

CAL-1 cells (if not otherwise indicated: 100,000 cells/well in a 96-well plate) were primed with hIFN-γ (10 ng/ml) for 6 hours prior to stimulation. J774 mouse macrophages (55,000 cells/well in a 96-well plate) were primed with mIFN-γ (20 ng/ml) for 6 hours prior to stimulation. BLaER1 cells (80,000 cells/well in a 96-well plate) as well as monocyte-derived macrophages (70,000 cells/well in a 96-well plate) were stimulated after trans-differentiation. Primary plasmacytoid dendritic cells (20,000 cells/well in a 96-well plate) were incubated with hIL-3 (10ng/ml) for 4 hours before stimulation.

For transfection with RNA9.2s (1.2 μg/well), $RNA40^O$ (1.2 μg/well), $RNA40^S$ (0.6μg/well) and short ORNs (CCUUCA$(dAdC)_7$, AAUUCA$(dAdC)_7$, UUUUUU$(dAdC)_7$) (2.4 μg/well), RNA and poly-L-arginine were incubated separately in a 1:1 ratio for 5 minutes in pre-warmed Opti-MEM (25 μl/well). Subsequently, the two reagents were combined and incubated for additional 20 minutes and afterwards added to the cells. For RNA transfections in the presence of the TLR8 inhibitor, CU-CPT9a was added 30 min prior to the stimulation (final concentration: 10 μM). If not otherwise indicated, cells were further stimulated with 200 ng/ml LPS-EB ultrapure, 1 μg/ml R848, 100 ng/ml TL8-506, 5 μM CpG^S, 5 μM CpG^O DNA or indicated concentrations of 2',3'-cGMP, 3'-GMP and 5'-GMP. Supernatants of CAL-1 cells and primary monocyte-derived macrophages were harvested after 16 hours of incubation at 37 °C and the supernatants of BLaER1 and J774 cells were harvested after 14 hours.

Isolation of PBMCs, primary plasmacytoid dendritic cells and primary human monocytes

Peripheral blood mononuclear cells (PBMCs) were isolated from the leukocyte reduction system chambers left over from platelet donation from healthy donors. Approval from the relevant ethics committee and informed consent from all donors according to the Declaration of Helsinki were obtained (project number: 19-238, Ethics Committee of the Medical Faculty of Ludwig-Maximilians-University Munich). PBMCs were isolated using BioColl and erythrocyte lysis (RBC lysis buffer). Human monocytes were MACS purified from PBMCs using CD14 microbeads and primary plasmacytoid dendritic cells were MACS purified with CD34 microbeads.

CRISPR/ Cas9 mediated knockout generation

Knockouts of CAL-1 cells and J774 macrophages were generated with RNPs. For CAL-1 monoclones the following gRNAs were used: TLR7 gRNA1: 5'-ACTGTGTACCTATTCCACTG-3'; gRNA2: 5'-CAGCTACTAGAGATACCGCA-3', PLD3 gRNA1: 5'-TAGCGGG TGTCATAGAACCG-3'; gRNA2: 5'-CCAGAGCAGGGGTTCCATTG-3', PLD4 gRNA1: 5'-GCAGTGCCAACATGGACTGG-3'; gRNA2: 5'-CCCATGGGGCGGCTCACCAG-3', RNase T2 gRNA1: 5'-ATCCTCACAGGAAGCATGAG-3'; gRNA2: 5'-GTTGAGCGCATCCAC CTGGG-3'. For the PLD3xPLD4 pool knockout of CAL-1 cells the same PLD3 guides were used but the PLD4 gRNAs were exchanged to: gRNA1: 5'-TGGGAGCGCTGGCTGTGCTG-3' and gRNA2: 5'-GACGGGGCACUUGCCACAGG-3'. For the PLD3 pool KO in J774 cells the following three gRNAs were used: gRNA1: 5'-CCACUCCACAGAAAGCCCGC-3', gRNA2: 5'-CACC GAAGCCCACUACCGCC-3' and gRNA3: 5'-CAGCUGUUUCUAUGGGAAUA-3'.

For CRISPR/Cas9 RNP assembly, crRNA and tracrRNA were incubated in a 1:1 molar ratio for 5 min at 95°C followed by incubation at room temperature for 1h. To each gRNA complex (100 pmol) NLS-Cas9 (40 pmol) was added and incubated for 15 minutes at room temperature. gRNA/Cas9 mixtures were once frozen at –80°C before usage. For nucleofection, $1x10^6$ CAL-1 cells or $2x10^5$ J774 macrophages were resuspended in 20 μl of SG Cell Line Nucleofector Solution. Cas9/RNP assembly was added and CAL-1 cells were nucleofected on a 4D-Nucleofector (Lonza) with the following program: DN-100. For J774 the program: CM-139 was used for nucleofection. Cells were transferred into 2 ml of pre-warmed culture medium. CAL-1 cells were rested for 24 hours before subjected to limiting dilution to obtain monoclones.

BLaER1 monocytes were gene targeted with the plasmid based CRISPR system. Here, the following gRNAs were used: PLD3 gRNA: 5'-TGCGGACGTTCACGCCCTT-3', PLD4 gRNA: 5'-GCCACGTGGACGCTCTCCT-3', TLR7 gRNA: 5'-ATGGGGCATTATAA CAACGA-3', TLR8 gRNA: 5'-CAGGAAGTTCCCCAAACGGT-3'. To $2.5x10^6$ cells in 250 μl of warm Opti-Mem medium 5 μg of

DNA (pCAS9-mCherry-gRNA) was added. The mixture was incubated for 15 min at room temperature and afterwards electroporated according to the following protocol: 265 V, 975 μF; 720 Ω using a Gene Pulser (BioRad). Cells were transferred into 2 ml of BLaER1 culture medium and rested for 24 hours. Using FACS analysis, mCherry positive cells were selected and monoclones were generated by limiting dilution. After three to four weeks, monoclones of CAL-1 and BLaER1 cells were picked and analyzed by MiSeq as described before.[40] Pool knockouts of CAL-1 and J774 cells were confirmed with the ICE CRISPR analysis tool from Synthego. For all cell lines, the parental cell line was used as wild-type controls.

CRISPR/ Cas9 mediated knockout generation in primary human monocytes

The same guide RNAs used to generate the *PLD3* x *PLD4* pool knockout in CAL-1 cells were also employed for knockouts in primary human monocytes. TBX21 gRNAs (gRNA1: 5'-CGTCCACAAACATCCTGTAG-3' gRNA2: 5'-GCGGTACCAGAGCGGCAAGT-3') were used as non-targeting controls. Pan monocytes were isolated from PBMCs by negative selection using the PAN Monocyte Isolation Kit. Immediately after isolation, cells were washed twice with PBS and $4x10^6$ cells were resuspended in 20 μl of P3 Nucleofector Solution. Cas9/RNP assembly was added and cells were nucleofected on a 4D-Nucleofector (Lonza) with the following program: EH-100. Immediately after nucleofection, cells were transferred into warm culture medium supplemented with M-CSF for differentiation. After 7 days, cells were counted and re-plated into 96-well plates. Stimulation was conducted on day 8 after nucleofection and knockout efficiencies were confirmed with the ICE CRISPR analysis tool from Synthego.

Lentiviral transduction

PLD3 was amplified from cDNA derived from BLaER1 cell lysate and cloned into a pFUGW_Blasticidin plasmid by Gibson cloning. CAL-1 cells were transduced for 48 h and afterwards selected with blasticidin (10 μg/ml). The polyclonal cell population was used for further experiments.

METHOD DETAILS

Immunoblotting

Samples were lysed in DISC buffer (150 mM NaCl, 50 mM Tris pH 7.5, 10% glycerol, 1% Triton X-100) supplemented with cOmplete protease inhibitor cocktail for 10 minutes on ice and afterwards centrifuged for 10 minutes at 16,000 g. The supernatant was collected, mixed with 6x Laemmli buffer (60 mM Tris pH 6.8, 9.3% DTT (w/v), 12% SDS (w/v), 47% glycerol (v/v), 0.06% bromphenol blue (w/v)) and denatured for 5 minutes at 95 °C. Samples were separated by TRIS glycine SDS-PAGE and transferred onto 0.45 mm nitrocellulose membrane. Next, membranes were blocked in 5% milk for 1 hour at room temperature and afterwards incubated with indicated primary and corresponding secondary antibodies. Chemiluminescent signals were recorded with a CCD camera.

ELISA

hIFN-β, hIFN-α2, hIL-6, hTNF and mIL-6 ELISAs were conducted according to supplier's protocol.

Gene expression analysis

Gene expression data shown in Figure 2A were obtained from the Human Cell Atlas (ImmGen Consortium; GEO: GSE227743). Data represent normalized gene counts of bulk RNA-Seq data from sorted cell populations from two healthy human blood donors.

PLD3 and PLD4 protein purification

Human PLD3 and human PLD4 were amplified from cDNA derived from BLaER1 cell lysates. PLD3 and PLD4 lacking the N-terminal domain and the transmembrane domain were fused to the Igκ leader sequence and a 6x His-tag and cloned into the piggyBac vector system,[41] followed by electroporation into RCH-ACV cells using a Gene Pulser device (BioRad). Stable pools of RCH-ACV cells expressing PLD3, PLD4 or various PLD3 mutants were generated by selection with blasticidin (10μg/ml) and puromycin (2.5 μg/ml).

Selected cells were grown to a density of $4x10^6$ cells/ml and protein expression was induced by exchanging the culture media into advanced RPMI 1640 medium, supplemented with doxycycline (1 μg/ml). Supernatants, containing the secreted proteins, were harvested and sterile filtered when cells viability decreased to 60%.

NI-NTA agarose beads were added to the supernatants and rotated overnight at 4 °C. Beads were washed three times with wash buffer (50 mM NaH_2PO_4, 300 mM NaCl, 10 mM Imidazol, pH=8.0) and eluted (50 mM NaH_2PO_4, 300 mM NaCl, 300 mM Imidazol, pH=8.0). The eluted proteins were concentrated and subjected to size exclusion chromatography (Superdex200) in the following buffer: 30 mM HEPES, 100 mM NaCl, pH=7.2. Fractions containing human PLD3 or human PLD4 were combined, concentrated and flash frozen with liquid nitrogen.

For purification of PLD3 and all PLD3 mutants (except for PLD3(H201N, H416N)), an additional cleavage site was introduced between the His-tag and the protein sequence to get rid of the His-tag before the proteins were subjected to size exclusion chromatography using a PreScission Protease. All protein concentrations were determined by BCA protein assay according to manufacturer's protocol.

Coomassie staining of PLD3 and PLD4

To analyze purity of recombinant PLD3 and PLD4, proteins were separated on a 12% TRIS glycine SDS-PAGE. The gel was afterwards stained with Coomassie (45% Ethanol, 10% acetic acid and 1g/L Coomassie Brilliant Blue R-250 Dye in milliQ water) for 1 h at room temperature and destained (20% Ethanol, 10% acetic acid in milliQ water) overnight.

Cryo-EM sample preparation and data acquisition of PLD3 and PLD4

Cryo EM experiments of active human PLD3 and PLD4 were conducted in a buffer containing 50 mM MES pH 5.5 and 100 mM NaCl (apo structure) or in a buffer containing 50 mM MES pH 5.5 and 50 mM NaCl (Ligand-bound PLD3). The proteins were diluted to a concentration of 0.5 mg/ml prior to grid preparation. For ligand bound sample preparation with RNA $(rU^*rC^*)_{10}$ or DNA $(A^*C^*)_{10}$, RNA or DNA was added to PLD3 in a 1:4 molar ratio (Protein:RNA/DNA) and incubated for 10 seconds at room temperature right before plunge freezing. For vitrification 4.5 μl sample was applied onto a glow discharged QUANTIFOIL® R2/ 1 Cu200 grid. The sample was vitrified in liquid ethane using an EM GP plunge freezer (Leica) at 15 °C and 95% humidity. Cryo-EM data collection was carried out using an FEI Titan Krios G3 transmission electron microscope (300 kV) equipped with either a Gatan energy filter equipped with a GIF quantum energy filter (slit width 20 eV) and a Gatan K2 Summit direct electron detector (software used: EPU 2.12.1.278REL, TEM User interface Titan 2.15.4, Digital Micrograph 3.22.1461.0) or a SelectrisX energy filter (slit width 10 eV) and a Falcon 4 direct electron detector (software used: EPU 3.5.1.6034). For the structure of PLD3 apoenzyme 10.755 movies were collected with the K2 summit setup with a total electron dose of 45 e^- Å^{-2}, fractionated into 40 movie frames. For the structure determination of PLD3 in complex with ssRNA 27.504 movies were collected with a total electron dose of 60 e^- Å^{-2}, fractionated into 60 movie frames. The datasets were collected with defocus values ranging from -0.5 to -2.8 μm and a pixel size of 1.045 Å for apoenzyme PLD3 and 0.727 Å for PLD3 in complex with ssRNA, respectively. Cryo-EM image processing movie frames were motion corrected using the Relion 4 implemented version of MotionCor2. All subsequent cryo-EM data processing steps were carried out using cryoSPARC 4.3.0[42] and the resolutions reported here are calculated based on the gold-standard Fourier shell correlation criterion (FSC = 0.143). The CTF parameters of the datasets were determined using patch CTF estimation. The exact processing schemes are depicted in Figure S4. The data collection and refinement statistics are summarized in Table S2. Particles were initially picked using Blob picker. Reasonable 2D classes were selected and used as input for Topaz train.[43] The resulting Topaz model was used as template for particle picking on all micrographs yielding 4.091.179 particles extracted with a box size of 300 px and a pixel size of 1.045 Å. The particles were subject to 2D classification, ab-initio reconstruction, and the class with clearly defined features was selected. The obtained particles were further sorted by 2D classification. The classes that showed the most defined features of PLD3 were selected (2.823.826 particles) and used for further non-uniform and CTF refinement.[42] The final resolution of the PLD3 reconstruction after non-uniform refinement applying C2 symmetry was 2.82 Å by masking out the flexible density presumably corresponding to glycosylation.

Cryo-EM data processing of PLD3 ssRNA complex was carried out in a similar fashion compared to the PLD3 apoenzyme dataset. In brief, for the complex data set particles were initially picked on 27.619 micrographs using blob picker, 2 classification and subsequent Topaz training and particle extraction. Particles corresponding to ssRNA bound classes were sorted and extracted with a box size of 330 px and a pixel size of 0.727 Å. Particles were further sorted by 2D classification, ab-initio reconstruction, and 3D classification. A total of 891.893 particles were combined and subjected to local Ctf refinement and non-uniform refinement. The final resolution of the PLD3 ssRNA bound reconstruction using C1 symmetry was 3.57 Å.

Model building and refinement

An atomic model was built by rigid body docking of the PLD3 dimer predicted by AlphaFold2[26] multimer into the cryo-EM density. The model was partially rebuilt in Coot 0.9.[44] Missing parts were built de-novo. Atomic models were improved by ISOLDE 1.2.244[45] and real space refinement in PHENIX 1.1745,[46,47] using the map with the highest resolution. All structure figures were prepared using UCSF ChimeraX.[48]

Mass photometry

Mass photometry measurements of PLD3, PLD4 and PLD3 mutants were carried out using a OneMP or TwoMP mass photometer (Refeyn). Proteins were diluted to a final concentration of 50 nM in sterile filtered mass photometry buffer (50 mM NaAC, 100 mM NaCl, pH 4.5) prior to each measurement. Movies were recorded for 60 s and data were analyzed using AcquireMP.

Nuclease assays

If not otherwise indicated 100 ng of RNA or DNA were digested with indicated enzyme concentrations for 20 min at 37°C in assay buffer (50 mM NaAc, 100 mM NaCl, pH 4.5). Afterwards, 2x RNA loading dye was added and samples were incubated for additional 5 min at 95 °C. Fragments were separated and visualized on a urea gel.

Urea gels

Urea gels were casted according to supplier's protocol using SequaGel Concentrate, SequaGel Diluent and SequaGel Bufffer. Gels run at 150 V for 10 min, followed by 250 V for 60 min in 1x TBE (100 mM Tris, 100 mM boric acid, 2 mM EDTA) buffer. Afterwards, gels were stained with SYBR Gold Nucleic Acid Gel Stain for 5 minutes and imaged.

Affinity measurement by fluorescence anisotropy

Fluorescence anisotropy experiments were conducted in a black flat bottom 384 well plate (50 μl total volume). 5 nM of 3'-FAM coupled substrates were incubated with increasing concentrations of indicated PLD3 mutants for 20 minutes at room temperature in assay buffer (50 mM NaAc, 100 mM NaCl, pH=4.5) to ensure equilibrium. Subsequently the change in anisotropy was measured at an excitation wavelength of 490 nm and an emission wavelength of 520 nm using an automated polarization microscope.[49] Each sample was measured at twelve different z-planes to reduce the effect of potential fluorescing protein-DNA aggregates that could lead to erroneous FA values. Data was analyzed by fitting to a one site-specific binding model.

Fluorescent RNA degradation assay

1 pmol/μl of fluorophore/quencher labeled RNA40 (5'-FAM fluorochrome/3'-BMN-Q530, Biomers) was mixed with indicated enzyme concentrations of PLD3 or PLD4 in assay buffer (50 mM NaAc, 100 mM NaCl, pH=4.5) in a black 96-well plate on ice (final reaction volume: 100 μl). FAM fluorescent signal (excitation 485 nm/emission 528 nm) was recorded on a Spark20M (Tecan) reader in 1 min intervals for 2 hours at 37°C.

PLD3 and PLD4 quantification and whole proteome analysis

$1x10^6$ cells (pDCs, $CD14^+$ and CAL-1 WT or KO cells) were washed 5 times with PBS. Cells lysis was performed in 8 M urea/0.4 M NH_4HCO_3 with a Sonopuls HD3200 ultrasonication device (Bandelin, Berlin, Germany). For protein quantification, a Bradford assay was used. Prior to tryptic digestion, 20 μg protein from each sample were reduced with dithiothreitol (final concentration 5 mM) at 37°C for 30 min and alkylated with iodoacetamide (15 mM final concentration) for 30 min at room temperature in the dark. The first digestion step was performed for 4 h with Lys-C (1:100, enzyme:protein -ratio). For additional tryptic digestion, samples were diluted with water to give 1 M Urea and digested overnight at 37°C with modified porcine trypsin (1:50, enzyme:protein-ratio). For absolute quantification of PLD3 and PLD4, 10 fmol of the following stable isotope labeled peptides were added to 1 μg of digested sample: PLD3: ALLNVVDNAX (A310 to R319), LFVVPADEAQAX (L397 to R408) and SQLEAIFLX (S458 to R466); PLD4: LQQLLGX (L164 to R170) and FWVVDGX (F217 to R223), with X being an Arginine labeled with 6 ^{13}C and 4 ^{15}N atoms. Purity of the internal standard peptides was evaluated using mass spectrometry.

For liquid chromatography mass spectrometry analysis, an UltiMate 3000 nano-LC system online coupled to a Q-Exactive HF-X instrument (Thermo Fisher Scientific) was used. As solvent A, 0.1% formic acid in water and as solvent, B 0.1% formic acid in acetonitrile were used. 1 μg of peptides dissolved in solvent A was injected to a PepMap 100 C18 trap column (100 μm × 2 cm, 5 μm particles) and separated on an analytical column (PepMap RSLC C18, 75 μm × 50 cm, 2 μm particles) at 250 nl/min flow-rate. The chromatography method consisted of an 80 min gradient of 5–20% of solvent B followed by a 9-min increase to 40%. After separation, the column was washed with 85% solvent B for 9 min and re-equilibrated for 10 min with 3% solvent B. For mass spectrometry analysis a data-independent acquisition (DIA) method was used as described in Shashikadze et al.[50] Briefly gas phase fractionation-based libraries were constructed using 6 measurements of pooled samples with 6 different scan ranges (i.e. 400.43–502.48, 500.48–602.52, 600.52–702.57, 700.57–802.61, 800.61–902.66, 900.66–1002.70) and staggered 25 × 4 m/z-wide isolation windows. For the analytical runs staggered 50 × 12 m/z-wide isolation windows in the range of 400–1000 *m/z* were used. Every 50 DIA scan was followed by a precursor scan in the range of 390–1010 *m/z*.

For the whole proteome analysis, first a gas phase fractionation spectral library was generated using DIA-NN (v1.8.1)[51] and all human Swiss-Prot entries as database. All raw files of the analytical runs were then searched against this library. For both searches, only tryptic peptides with a maximum of one missed cleavage, a length between 7 and 30 amino acids and charge states of either +2, +3 and +4 were considered. Proteins were grouped in the output based on their gene names. For the quantitative analysis of PLD3 and PLD4, the Skyline ecosystem was used.[52] For each peptide, three product ions were selected and a minimum of rdotp = 0.85 was required of each individual peptide identification. As normalization method, "ratio to heavy" was chosen.

Preparation for LC-MS analysis of PLD3 and PLD4 degradation products

To analyze cleavage products of PLD3 and PLD4 *in vitro*,1 μg of $RNA40^O$ or $RNA9.2s^O$ was incubated with indicated concentrations of PLD3, PLD4, RNase T2, RNase 1, RNase 2 or RNase 6 or combinations thereof at 37°C in assay buffer (50 mM NaAC, 100 mM NaCl, pH 4.5). Next, proteins were precipitated in 80% acetonitrile for 30 min on ice and centrifuged for 10 min at 16,000 g. To detect nucleosides in cells, $3x10^6$ CAL-1 cells were primed with IFN- γ (10 ng/μl) for 6 hours and stimulated with $RNA40^O$ as described above for additional 16 hours. Subsequently, cells were lysed in 80% acetonitrile for 30 min on ice and centrifuged for 10 min at 16,000 g. The supernatants (from *in vitro* and cell studies) were collected, flash frozen in liquid nitrogen and lyophilized overnight. The pellets were dissolved in 50 μl ultrapure water and stored at -20 °C if necessary. Prior to analysis the sample was centrifuged at 10,000 ×g for 1 min and the amount indicated for the respective analysis below was taken from the upper part of the liquid.

LC-MS/QQQ analysis of nucleoside-monophosphates

For semi-quantitative mass spectrometry of nucleoside-monophosphates an Agilent 1290 Infinity HPLC equipped with a variable wavelength detector (VWD) combined with an Agilent Technologies G6490 Triple Quad mass spectrometer with electrospray ionization (ESI-MS, Agilent Jetstream) was used. Operating parameters were as follows: positive-ion mode, cell accelerator voltage of 5 V, N_2 gas temperature of 150 °C and N_2 gas flow of 20 l/min, sheath gas (N_2) temperature of 400 °C with a flow of 12 L/min, capillary voltage of 2400 V, nozzle voltage of 0 V, nebulizer at 60 psi, high-pressure RF at 180 V and low-pressure RF at 80 V. The

instrument was operated in dynamic MRM mode with a cycle time of 700 ms (Table S2). For separation an Interchim Uptisphere 120 Å column (HDO-C18, 3 μm, 2.1 × 150 mm, UP3HDO-150/021) was used. Running conditions were 35 °C and a flow rate of 0.35 ml/min in combination with a binary mobile phase of 5 mM NH_4OAc aqueous buffer A, brought to pH 4.9 with glacial acetic acid (200 μL/L), and an organic buffer B of acetonitrile (Ultra LC-MS grade, purity ≥99.98) acidified with 0.075 % formic acid (187.5 μl per 2.5 l). The used gradient is described below. Of each sample 15 μl were diluted with 15 μl of buffer A and 20 μl of this solution was then co-injected with 1 μl of stable isotope labeled internal standard (ISTD) mix which was aspirated automatically before each injection from the instrument itself and consisted of isotopologues of the 4 canonical nucleosides. The sample data were analyzed by the quantitative MassHunter Software from Agilent using the integrated calibration function. The calibration solutions ranged from 0.01 pmol to 25 pmol for each nucleoside (12 calibration levels, 1:2 dilution). The amount of nucleoside-monophosphates was normalized by the average of the relative amounts of canonical nucleosides. For example, the amount of C in each sample was normalized to the amount of control sample #1. The same was done for U, G and A. Finally, the normalized values for C; U, G and A were averaged and used for normalization of the nucleoside-monophosphates. This normalization method is intended to compensate for fluctuations between the different samples as best as possible while only using highly aberrant nucleoside species.

The gradient was as follows: 0 → 0.75 min, 0% B; 0.75 → 1.50 min, transition to 2.5% B; 1.50 → 3.00 min, 2.5% B; 3.00 → 8.00 min, transition to 15% B; 8.00 → 9.00 min, transition to 80% B; 9.00 → 11.50 min, 80% B; 11.50 → 12.00 min, transition to 0% B; 12.00 → 13.70 min, 0% B.

LC-HRMS analysis of oligonucleotides

A Thermo Scientific Vanquish system coupled to a Thermo Scientific QExactive HF mass spectrometer was used for the high-resolution mass spectrometry (HRMS) analysis of oligonucleotides and their fragments. Ionization was done by a HESI source and ions were scanned in the positive polarity mode over a full-scan range of m/z 200-1600 with a resolution of 120,000, an AGC target of 3e6 and a maximum IT of 200 ms. HESI Tune parameters are: Capillary temperature 320 °C, sheath gas flow rate 20 au, aux gas flow rate 4 au, sweep gas flow rate 0 au, spray voltage 3.5 kV, S-lens RF level 50, aux gas temperature 55 °C. Fragments were separated on a Macherey-Nagel Nucleodur HILIC column (EC125/2, 3 μm, 2 × 125 mm, 760531.20) at 40 °C. Elution buffers were 10 mM NH_4OAc aqueous buffer A, brought to pH 5.3 with glacial acetic acid (65 μL/L) and an organic buffer B of 10 mM NH_4OAc brought to pH 5.3 with glacial acetic acid in 80 % acetonitrile (Ultra LC-MS grade, purity ≥99.98) with a flow rate of 0.30 ml/min. The buffer-gradient is described below. For each measurement 10 μl of sample was spiked with 1 μl of an ISTD-mixture of ^{13}C-labeld C, U, G and A (each of them at a concentration of 10 μM) and diluted with 50 μl of buffer A. Of this solution 20 μl were subjected to HRMS. The ion chromatograms of intact oligonucleotides and their fragments were extracted from the total ion current (TIC) chromatogram. The gradient was as follows: 0.0 → 2.0 min, 100% B; 2.0 → 22.0 min, transition to 60% B; 22.0 → 27.0 min, transition to 25% B; 27.0 → 31.0 min, 25% B; 31.0 → 33.0 min, transition to 100% B; 33.0 → 44.0 min, 100% B.

QUANTIFICATION AND STATISTICAL ANALYSIS

Unless otherwise indicated, statistical significance was determined by either one-way or two-way ANOVA with Dunnett's correction for multiple testing. The exact number of replicates (n) is given in the figure legends. GraphPad Prism 10 was used for data presentation and statistical analysis. When multiple comparisons are displayed with a comparison bar, the longer line on the comparison bar indicates the reference data to which the significance level information relates.